ARHGAP17 regulates the spatiotemporal activity of Cdc42 at invadopodia

Gabriel Kreider-Letterman[1], Abel Castillo[1], Eike K. Mahlandt[2], Joachim Goedhart[2], Agustin Rabino[1], Silvia Goicoechea[1], and Rafael Garcia-Mata[1,*]

[1]Department of Biological Sciences, University of Toledo, Toledo, Ohio, USA

[2]Swammerdam Institute for Life Sciences, Section of Molecular Cytology, van Leeuwenhoek Centre for Advanced Microscopy, University of Amsterdam, Amsterdam, The Netherlands

*Corresponding author: rafael.garciamata@utoledo.edu

Abstract

Invadopodia formation is regulated by Rho GTPases. However, the molecular mechanisms that control Rho GTPase signaling at invadopodia remain poorly understood. Here, we have identified ARHGAP17, a Cdc42-specific RhoGAP, as a key regulator of invadopodia in breast cancer cells and by RhoGAPs characterized a novel ARHGAP17-mediated signaling pathway that controls the spatiotemporal activity of Cdc42 during invadopodia turnover. Our results show that during invadopodia assembly, ARHGAP17 localizes to the invadopodia ring and restricts the activity of Cdc42 to the invadopodia core, where it promotes invadopodia growth. Invadopodia disassembly starts when ARHGAP17 translocates from the invadopodia ring to the core, in a process that is mediated by its interaction with the Cdc42 effector CIP4. Once at the core, ARHGAP17 inactivates Cdc42 to promote invadopodia disassembly. Our results in invadopodia provide new insights on the coordinated transition between the activation and inactivation of Rho GTPases.

Introduction

The risks associated with cancer metastasis makes breast cancer one of the leading causes of cancer related mortality among women. One way that metastatic cancer cells invade tissues is through the formation of protrusive, actin-rich structures called invadopodia, which mediate the degradation of the extracellular matrix (ECM) (Murphy and Courtneidge, 2011). The ability of cancer cells to form invadopodia has been correlated with their metastatic potential, and the loss of invadopodia with decreased tumorigenicity and dissemination (Meirson et al., 2018; Stoletov and Lewis, 2015; Yamaguchi, 2012). In addition, studies using intravital microscopy have documented the existence of invadopodia and confirmed their importance for intra/extravasation and dissemination *in vivo* (Gligorijevic et al., 2014).

The structure of invadopodia is typically comprised of an actin-rich core that is surrounded by a ring of adhesion and scaffolding proteins, like that of podosomes which occur in normal cells (Murphy and Courtneidge, 2011). Invadopodia form through a series of steps that is initiated by the disassembly of focal adhesions and stress fibers, and the recycling of many of their components into new invadopodia (Hoshino et al., 2012; Oikawa et al., 2008). Assembly of new invadopodia starts with the formation of actin- and cortactin-rich puncta, closely followed by the recruitment of adhesion proteins such as vinculin and paxillin (Hoshino et al., 2013). Invadopodia reach maturity upon the recruitment of matrix metalloproteases which facilitate matrix degradation (Hoshino et al., 2013). There is less known about

the steps of invadopodia disassembly although the Rho GTPase RhoG and tyrosine phosphorylation of paxillin have been implicated in the process (Badowski et al., 2008; Goicoechea et al., 2017).

The dramatic rearrangement of the actin cytoskeleton during invadopodia formation is regulated by the Rho family of small GTPases (Murphy and Courtneidge, 2011). Rho GTPases function as molecular switches that cycle between an active GTP-bound and an inactive-GDP bound state. The activation of Rho proteins is catalyzed by RhoGEFs (guanine nucleotide exchange factors), whereas RhoGAPs (GTPase-activating proteins) mediate their inactivation. There are 80 RhoGEFs and 66 RhoGAPs in humans, allowing cells to tightly regulate the activity of Rho proteins through multiple pathways (Kreider-Letterman et al., 2022a; Rossman et al., 2005). Since RhoGAPs play a critical role in the termination of signal transduction, mutations in genes encoding RhoGAPs have drastic consequences and underlie several human diseases including cancer (Kreider-Letterman et al., 2022a). RhoGAPs are generally considered tumor suppressors, and the loss of GAP activity results in aberrant GTPase activity which can promote tumorigenesis (Kreider-Letterman et al., 2022a). However, compared with RhoGEFs, which have been studied more extensively, there is significantly less known about RhoGAPs, especially regarding their role in cancer progression and metastasis. The need to better characterize RhoGAPs in cancer progression includes invadopodia as there is increasing evidence that RhoGAPs play a role in their regulation (Al Haddad et al., 2020; Bravo-Cordero et al., 2011; Diring et al., 2019; Nakahara et al., 1998; Noll et al., 2019).

Several Rho proteins are known to be directly involved in invadopodia formation, including Cdc42, Rac1, RhoA, RhoC, and RhoG (Ayala et al., 2009; Bravo-Cordero et al., 2011; Goicoechea et al., 2017; Moshfegh et al., 2014; Sakurai-Yageta et al., 2008; Yamaguchi et al., 2005). However, the molecular mechanisms of their spatiotemporal activity at invadopodia, as well as the identity of their upstream regulators and downstream effectors remain poorly characterized. Here, we conducted a candidate shRNA screen to find RhoGAPs involved in invadopodia formation and identified ARHGAP17 (RICH1, Nadrin), a Cdc42-specific GAP and a negative regulator of invadopodia in triple negative breast cancer cells.

Using TIRF and STORM microscopy and live cell analysis of Cdc42 activity via biosensors, we found that during invadopodia assembly, ARHGAP17 localizes specifically to the ring region of invadopodia where it functions to restrict the activity of Cdc42 to the invadopodia core. Interestingly, invadopodia start to disassemble when ARHGAP17 translocates from the ring to the core where it inactivates Cdc42 and promotes invadopodia disassembly. We also show that this shift in localization is mediated by the interaction between ARHGAP17 and CIP4, a Cdc42 effector which localizes to the core of invadopodia and is important for invadopodia assembly. Altogether, our results identify ARHGAP17 at the center of the dynamic regulation of invadopodia assembly and disassembly and provide new insights into the molecular mechanisms controlling these processes.

Results

ARHGAP17 is a negative regulator of invadopodia in breast cancer cells

To characterize the role of RhoGAPs during invadopodia formation, we used the triple negative breast cancer (TNBC) cell line SUM159 as a model. SUM159 cells produce invadopodia that are highly dynamic and typically form in clusters under the nucleus or as bands at the leading edge (Fig. 1 A and Video 1) (Goicoechea et al., 2017). When grown in culture, the cells form invadopodia clusters spontaneously at low levels (≈1% cells) (Fig. S1 B). However, treatment with the phorbol ester Phorbol 12,13-dibutyrate

80 (PDBu) stimulates the formation of large numbers of invadopodia, with about 30% of cells forming
81 invadopodia after 30 minutes (Video 1) (Goicoechea et al., 2009; Goicoechea et al., 2017). To identify
82 RhoGAPs that may regulate invadopodia formation, we performed an shRNA screen on a panel of
83 candidate RhoGAPs in PDBu treated SUM159 cells (Fig. 1 B). We tested 19 RhoGAP candidates using 5
84 targeting sequences per gene. Several RhoGAPs showed differences in the percentage of cells with
85 invadopodia, typically an increase. Here, we focused on ARHGAP17, as silencing its expression showed
86 the most prominent increases in the percentage of cells forming invadopodia, especially with shRNA
87 sequences #3 and #5. We confirmed the efficiency of the shRNA targeting sequences by western blot
88 analysis, which shows a significant reduction of ARHGAP17 expression in both sequences #3 and #5
89 when compared to the non-targeting control (Fig. 1 C). We also repeated the invadopodia assay with
90 both shRNA sequences and confirmed that depletion of ARHGAP17 resulted in significant increases in
91 the number of cells that form invadopodia after PDBu treatment (from 28.7% in CTRL cells to 79.3% and
92 72.3% in shRNAs #3 and #5 respectively) (Fig. 1 D). We also observed similar results using two unique
93 CRISPR KO sequences for ARHGAP17 (Fig. S1 A and B). In addition, we were able to rescue the effects of
94 silencing ARHGAP17 on invadopodia by re-expressing an shRNA resistant myc-ARHGAP17 (Fig. 1 E-G).
95 The increase in cells forming invadopodia observed in ARHGAP17 KD was independent of PDBu
96 treatment as silencing ARHGAP17 also induced a significant increase in the number of spontaneous
97 invadopodia in untreated cells (from 1.3% in CTRL cells to 7.8% in ARHGAP17 KO) (Fig. S2 A and B). These
98 results validated the specificity of the phenotype and demonstrated that the effect of silencing
99 ARHGAP17 expression is not dependent on PDBu treatment. Taken together our results suggest that
100 ARHGAP17 functions as a negative regulator of invadopodia.

101 **ARHGAP17 regulates invadopodia-based matrix degradation and inhibits invasion**

102 To determine whether the increases in invadopodia in the absence of ARHGAP17 resulted in more
103 invadopodia activity, we used a matrix degradation assay in which we plated SUM159 cells on a
104 fluorescent gelatin/collagen IV matrix and treated them with PDBu for 24 hours (Martin et al., 2012).
105 SUM159 cells degraded the matrix with a punctate pattern typical for invadopodia; characterized by F-
106 actin puncta overlapping with a loss of matrix fluorescence, provided the cell had not moved before
107 fixation (Fig. 2 A) (Artym et al., 2006). We quantified invadopodia activity in CTRL, ARHGAP17 KO, and
108 Rescue cells by measuring the area of degradation/cell area. We found a significant increase in matrix
109 degradation in ARHGAP17 KO cells (~3-fold) which was rescued to CTRL levels by re-expressing
110 ARHGAP17 (Fig. 2 B and C). These results demonstrate that the additional invadopodia formed in the
111 absence of ARHGAP17 are functional.

112 Since silencing the expression of ARHGAP17 results in increased matrix degradation via invadopodia, we
113 would predict the cells to be more invasive when grown in 3D. To determine if ARHGAP17 KD cells are
114 more invasive, we performed a 3D spheroid invasion assay (Vinci et al., 2015). In this assay, SUM159
115 cells were grown in ultra-low attachment plates that resulted in the formation of a spheroid reminiscent
116 of a small tumor (Fig. 2 D). When the spheroids are embedded in Matrigel, invasive cells migrate away
117 from the spheroid and into the matrix. Spheroid growth and invasion can then be quantified by
118 measuring the area of the spheroid over time. We found that even though ARHGAP17 KD spheroids
119 grew at a slower rate (Fig. 2 E), they were significantly more invasive when invasion was normalized by
120 average proliferation (Fig. 2 F). To validate the spheroid invasion results without the effect of growth
121 impacting the results we also performed an inverse invasion assay. In this assay, we plated SUM159 cells
122 stably expressing mScarlet-CAAX (membrane marker) at the bottom of a plate, overlaid them with a

123 layer of Matrigel and stimulated them to invade upwards by adding serum-containing media on top of
124 the Matrigel (Fig. 2 G and Video 2). Quantification showed that ARHGAP17 KO cells invaded significantly
125 more than the CTRL and that this effect was rescued by re-expressing ARHGAP17 (Fig. 2 H).

126 **ARHGAP17 regulates invadopodia dynamics**

127 The dramatic increase in invadopodia observed in ARHGAP17 KD cells suggested that ARHGAP17 could
128 be modulating invadopodia turnover. Interestingly, in the absence of ARHGAP17, not only were more
129 cells able to form invadopodia compared to CTRL cells, but also the invadopodia clusters were larger
130 (Fig. 3 A). This may reflect a change in invadopodia dynamics, possibly due to an increase in invadopodia
131 lifetime or defects in disassembly signaling. To further explore this possibility, we performed a time-
132 course experiment in which we treated SUM159 cells (CTRL, ARHGAP17 KD, and Rescue) with PDBu and
133 quantified the percentage of cells forming invadopodia at successive time points after treatment (Fig. 3
134 B). As we have previously described (Goicoechea et al., 2017), CTRL cells showed a rapid spike in
135 invadopodia forming cells at the 10-minute mark that then decreased rapidly until reaching equilibrium
136 at 30 minutes, with approximately 30% of cells being positive for invadopodia at any given time
137 afterwards. Interestingly, the initial increase in invadopodia was larger in ARHGAP17 KD cells (>80%
138 positive cells at 10 min), and the decrease not as pronounced, with invadopodia percentages reaching
139 an equilibrium at a much higher percentage (>60% after 30 min). Re-expressing ARHGAP17 restored the
140 normal time-course dynamics (Fig. 3 B). When we calculated the difference in percentage of cells with
141 invadopodia between the 10- and 30-min time points, i.e., the drop-off from peak to equilibrium, the
142 difference was significantly smaller in ARHGAP17 KD cells when compared to CTRL or Rescue (50%
143 reduction in CTRL vs. 20% reduction in ARHGAP17 KD) (Fig. S3 A). These results suggest that in the
144 absence of ARHGAP17, the invadopodia may be more stable and thus longer lived.

145 We next wanted to characterize the role of ARHGAP17 on invadopodia dynamics. The dynamics of single
146 invadopodia can be divided into three defined stages: assembly, stability, and disassembly. This is
147 illustrated in Fig. 3 C, in which the intensity of the invadopodia marker TKS5-mTagBFP2 was measured
148 over the lifetime of a single invadopodia. Using live Total Internal Reflection Fluorescence (TIRF)
149 microscopy and a custom algorithm inspired by a similar method previously used to quantify focal
150 adhesions (Berginski et al., 2011), we were able to accurately measure the dynamics of invadopodia
151 formation after PDBu treatment with high enough resolution to resolve the individual invadopodia from
152 the clusters (Fig. 3 D). Using this method, we found that individual invadopodia have increased overall
153 lifetime in ARHGAP17 KO cells (Fig. 3 D and E), and that this increase in lifetime was a result of an
154 increase in the duration of the stability phase (Fig. 3 H) and not due to significant changes in the
155 duration of the assembly or disassembly phases (Fig. 3 F and G). We also confirmed that the effect of
156 silencing ARHGAP17 on lifetime was independent of PDBu treatment, as we observed a similar increase
157 in lifetime in spontaneous invadopodia in the absence of ARHGAP17 (Fig. S4 A). Interestingly, we found
158 no significant changes in the assembly or disassembly rates (Fig. S4 B and C). Finally, we analyzed the
159 results using a Principal Component Analysis (PCA) which confirmed that ARHGAP17 KO invadopodia
160 form a distinct population based on lifetime and stability with only minimal impact from the other
161 variables (Fig. S4 D). These results demonstrate that ARHGAP17 regulates the dynamics of invadopodia
162 and that, in the absence of ARHGAP17, invadopodia are more stable which is associated with increased
163 accumulation of invadopodia within clusters.

164 **ARHGAP17 is targeted to invadopodia through multiple domains**

165 To visualize the localization of endogenous ARHGAP17 in cells we generated a polyclonal antibody
166 against a small peptide from the C-terminus of ARHGAP17. The antibody recognized a single band by
167 western blot, which disappeared upon KD or KO of ARHGAP17 (Fig. 1 C and Fig. S1 A). In PDBu-treated
168 SUM159 cells, the ARHGAP17 antibody showed a clear signal at the invadopodia clusters. This signal was
169 lost in ARHGAP17 KO cells confirming the specificity of the antibody (Fig. 4 A). A similar result was
170 observed when expressing an ARHGAP17-GFP construct in ARHGAP17 KO SUM159 cells, with
171 ARHGAP17-GFP targeting efficiently to invadopodia as marked by TKS5-mTagBFP2 (Fig. 4 B). Live
172 imaging analysis showed that ARHGAP17-GFP is recruited early during invadopodia formation, almost
173 simultaneously with TKS5-mTagBFP2, and remains associated until the invadopodia disappears (Fig. 4 B
174 and Video 3). Interestingly, we observed that ARHGAP17 did not perfectly colocalize with TKS5 and had
175 a more diffuse appearance with the signal localized in some cases adjacent to, or in the periphery of
176 TKS5 puncta (Fig. 4 B, zoom panel).

177 Invadopodia are typically organized with a core region comprised of actin, actin nucleators, and
178 scaffolding proteins, and a surrounding ring comprised of adhesion and adapter proteins such as paxillin
179 and vinculin (Branch et al., 2012). Our initial results suggested that ARHGAP17 may be localized
180 preferentially to the ring region of invadopodia. To better define the localization of ARHGAP17 at
181 invadopodia, we utilized STORM (Stochastic Optical Reconstruction Microscopy) reconstructions of
182 invadopodia using F-actin (phalloidin staining) and cortactin as markers for the invadopodia core, and
183 paxillin as a marker for the ring. We then compared the intensity distribution of these proteins to that of
184 myc-ARHGAP17. We used ARHGAP17 KO SUM159 cells stably expressing myc-ARHGAP17 to facilitate
185 the use of anti-myc antibodies, which provided better results with STORM than staining for the
186 endogenous protein. From these results, ARHGAP17 appears to share its localization pattern more with
187 paxillin than actin or cortactin (Fig. 4 C and Fig. S5 A and B).

188 To compare the localization of different invadopodia proteins we developed a semi-automatic macro
189 script in ImageJ that measures the intensity of invadopodia proteins in relation to the center of the
190 invadopodia (hereafter referred to as radial intensity analysis). In this script, a line is drawn across the
191 center of each invadopodia. The line is then sequentially rotated 120 times at 3° intervals and the
192 intensity profile is measured at each of the intervals for all fluorescent channels. The mean of all
193 measurements is then used to display the average intensity related to the distance from the center of
194 the invadopodia (Fig. 4 D). When this method is applied to the STORM reconstructions, we found that
195 ARHGAP17 localization extends further away from the center of the invadopodia when compared to the
196 core proteins cortactin and F-actin, and aligns closely with the ring protein paxillin, suggesting it is a ring
197 protein (Fig. 4 D). However, unlike paxillin, a fraction of ARHGAP17 is also localized to the core. Fig. 4 D
198 shows that the intensity of myc-ARHGAP17 remains high at the core when compared to that of paxillin,
199 which decreases sharply at the invadopodia center (Fig. 4 C and Fig. S5 A and B). An equivalent
200 localization of ARHGAP17 to the ring was also observed in the spontaneous invadopodia that form in
201 non-treated cells (Fig. S6 A and B).

202 To determine how ARHGAP17 is targeted to invadopodia, we generated and expressed a series of
203 domain deletion mutants in ARHGAP17 KO SUM159 cells (Fig. 5 A and Fig. S7 A). Using TIRF microscopy
204 for its high signal-to-noise ratio, we found that both the N-BAR domain and the C-terminus Proline-rich
205 region are important for targeting ARHGAP17 to invadopodia (Fig. 5 B-E). We then used the radial
206 intensity analysis to precisely define the localization for each of the mutants (Fig. 5 C). Our results show
207 that upon deletion of the C-terminus (ΔC), ARHGAP17 localization decreases at the core, but remains

208 associated with the ring, which suggests that the Proline-rich region is important for targeting
209 ARHGAP17 to the center of invadopodia (Fig. 5 B and C). In this mutant, the ring diameter is also wider
210 (Fig. 5 D). In contrast, when the N-BAR domain is deleted (ΔBAR), there is an increase in the localization
211 of ARHGAP17 to the core, which is accompanied by a slight reduction in the ring and a more diffuse
212 localization pattern (Fig. 5 B-D). Interestingly, the N-BAR domain alone is sufficient to target to the core
213 of invadopodia, where it is distributed in a punctate pattern (Fig. 5 B-E). Deletion of either the C-
214 terminus or the N-BAR domain reduced the total amount of ARHGAP17 recruited to invadopodia
215 compared to the WT protein, which suggests that targeting to invadopodia is partially compromised in
216 both mutants (Fig. 5 E).

217 We also tested these deletion mutants for their ability to rescue the ARHGAP17 KO phenotype. Our
218 results show that the ΔC mutant rescues the levels of invadopodia efficiently to a level that is close but
219 still significantly different than that of the WT Rescue. The ΔBAR mutant also showed a reproducible
220 level of rescue although it was less efficient than the ΔC mutant. In contrast, the N-BAR domain alone
221 showed no evidence of rescue, which confirms that the rest of the protein is not only important for
222 targeting but also for ARHGAP17's function. (Fig. 5 F). From these results, we conclude that ARHGAP17
223 regulates invadopodia by its ability to associate to both the ring and core structures through the N-BAR
224 domain and C-terminus, respectively.

225 **ARHGAP17 regulation of invadopodia requires its RhoGAP activity for Cdc42**

226 *In vitro* assays have initially shown ARHGAP17 to have RhoGAP specificity for all three of the ubiquitous
227 Rho GTPases: Cdc42, Rac1, and RhoA (Harada et al., 2000). However, later studies suggest it is specific
228 for Cdc42 and Rac1 *in vitro* with preference for Cdc42 in cells (Richnau and Aspenstrom, 2001; Richnau
229 et al., 2004; Wells et al., 2006). To assess the specificity of endogenous ARHGAP17 in SUM159 cells, we
230 performed a GAP pulldown assay using glutathione S-transferase (GST)-tagged, constitutively active
231 mutants of RhoA, Rac1, and Cdc42 (Fig. 6 A) (García-Mata et al., 2006). We found that ARHGAP17
232 precipitated with active Cdc42 but not with RhoA or Rac1. Furthermore, when the expression of
233 ARHGAP17 was silenced in SUM159 cells, there was a significant increase in total Cdc42 activity in the
234 cells as determined by an affinity pulldown assay (Fig. 6 B). From these results, we determined that in
235 SUM159 cells ARHGAP17 is specific for Cdc42.

236 Since Cdc42 signaling is known to be essential for the formation of invadopodia (Ayala et al., 2009; Di
237 Martino et al., 2014; Goicoechea et al., 2014; Sakurai-Yageta et al., 2008; Yamaguchi et al., 2005;
238 Zagryazhskaya-Masson et al., 2020), we performed a time course assay in which we measured Cdc42
239 activity in SUM159 cells at 10-minute intervals following PDBu treatment (Fig. 6 C). Our results showed a
240 peak in Cdc42 activity in CTRL cells that roughly correlates with the time course of invadopodia
241 formation (see Fig. 3 B). ARHGAP17 KD cells also showed an increase in Cdc42 activity at the same time
242 point (20 min). However, the Cdc42 increase was not as prominent as in CTRL cells, likely because the
243 basal activity of Cdc42 is already comparatively higher at time zero in the ARGHAP17 KD cells (Fig. 6 B
244 and Fig. S8 A, compare the activity between t0 and t20). These results suggest that ARHGAP17
245 modulates the activity of Cdc42 during the formation of invadopodia.

246 To test this prediction, we mutated the critical Arginine finger motif in the RhoGAP domain of
247 ARHGAP17 (R288A), which renders it catalytically dead (CD) (Harada et al., 2000). We then quantified
248 both the localization of ARHGAP17 CD to invadopodia and its ability to rescue the ARHGAP17 KO
249 phenotype. Our results demonstrated that the catalytic activity is not required for targeting ARHGAP17

250 to invadopodia, as the CD mutant localization and radial intensity analysis were indistinguishable from
251 that of the WT protein (Fig. 6 D and E and Fig. S9 A). The distance from the core and the intensity at the
252 invadopodia were also not significantly different between WT and CD ARHGAP17 (Fig. 6 F and G).
253 However, despite targeting correctly, the CD mutant was unable to rescue the KO phenotype, which
254 suggests the RhoGAP activity is required for ARHGAP17 to regulate invadopodia turnover (Fig. 6 H).

255 **Spatiotemporal regulation of Cdc42 by ARHGAP17 at invadopodia**

256 Since ARHGAP17 regulation of invadopodia requires its Cdc42-specific RhoGAP activity, we wanted to
257 characterize the spatiotemporal regulation of Cdc42 activity and ARHGAP17 at invadopodia. We initially
258 analyzed the dynamics of Cdc42 in live cells using a previously described Cdc42-FRET biosensor, which
259 we co-expressed in SUM159 cells with mCherry-cortactin as an invadopodia marker (Reinhard et al.,
260 2017). This unimolecular FRET sensor, and similar designs for Rac1 and RhoA, have been previously
261 characterized (Kedziora et al., 2016; Reinhard et al., 2017; Timmerman et al., 2015; van Unen et al.,
262 2016). The Cdc42 FRET biosensor behaved as previously described, showing higher Cdc42-activity at the
263 edge of dynamic cells protrusions, which are enriched in mCherry-cortactin (Fig. S10 A) (Machacek et al.,
264 2009). During invadopodia formation, again visualized with mCherry-cortactin, we observed an increase
265 in Cdc42 activity at invadopodia (Fig. S10 A). The FRET signal increased at invadopodia as they
266 assembled and decreased during their disassembly until returning to background levels (Fig. S10 B). To
267 determine whether we could map the FRET signal representing the activity to Cdc42 to the core or ring
268 of each invadopodia puncta, we applied the radial intensity analysis to compare the FRET biosensor
269 signal to the signal of mCherry-cortactin (core marker). Our results showed that the FRET signal broadly
270 overlaps with that of cortactin, suggesting the activity is mostly restricted to the core (Fig. S10 D).
271 However, the spatial resolution of the FRET sensor is significantly lower than that of mCherry-cortactin,
272 and the variability between individual puncta is high, so it was difficult to definitively conclude that
273 Cdc42 was only active at the core. To obtain higher resolution images of the dynamics of Cdc42 activity
274 in live cells, we took advantage of a localization based Cdc42 biosensor (dTomato-wGBD) that has been
275 recently optimized for imaging in mammalian cells. The sensor consists of the GTPase-binding domain of
276 the Cdc42 effector WASP (wGBD) linked to the dTomato fluorescent protein (Fig. S11 A). The sensor
277 encodes the Cdc42 binding domain of WASP only, so it does not interact with other WASP-binding
278 proteins such as Cdc42 effector proteins (e.g., CIP4), so the accumulation of signal in cells should reflect
279 its association with active Cdc42 pools (Tian et al., 2000). This sensor design has been extensively used in
280 the past, particularly in Xenopus studies, but was typically not sensitive enough for mammalian cell
281 studies (Benink and Bement, 2005; Kim et al., 2000; Vaughan et al., 2011). Our new Cdc42 sensor has
282 been designed using the same iterative approach we recently described for a RhoA sensor (Mahlandt et
283 al., 2021). To verify the specificity of the sensor in SUM159 cells, we used an assay that measures the
284 translocation of the sensor to the nucleus when co-expressed with different nuclear localized
285 constitutively active Rho GTPases as we have previously described (Mahlandt et al., 2021). Our results
286 show that the dTomato-wGBD sensor only relocates to the nucleus in the presence of constitutively
287 active Cdc42, suggesting it is highly specific for Cdc42 (Fig. S11 B). Quantification of nuclear over
288 cytosolic shows a >4-fold ratio increases when nuclear Cdc42 is expressed vs. the empty nuclear control.
289 Nuclear Rac1 showed only residual binding, while RhoA showed no detectable binding (Fig. S11 B and C).
290 Similarly to what has been reported when Cdc42 activity was measured using FRET sensors, the wGBD
291 sensor, but not the empty control sensor, localizes to the leading edge of protruding lamellipodia, and
292 its signal decreases upon retraction (Fig. S11 D and E and Video 4) (Machacek et al., 2009).

293 We then tested the localization of the sensor in SUM159 cells stimulated with PDBu to form
294 invadopodia. Upon treatment of PDBu, the sensor strongly re-localizes to newly forming invadopodia,
295 indicating an increase in Cdc42 activity specifically at invadopodia (Fig. 7 A and Video 5). In contrast, the
296 negative control showed no accumulation at invadopodia clusters (Fig. S12 A and Video 6). We also
297 followed the activity of Cdc42 in single invadopodia over time and compared it with the intensity of
298 ARGHAP17-GFP and TKS5-mTagBFP2. We found that the sensor signal follows the progression of the
299 invadopodia, increasing in intensity during its assembly and decreasing as the invadopodia disappears
300 (Fig. 7 B and Video 7). Interestingly, we observed that Cdc42 activity appears early during the initial
301 stages of invadopodia formation, overlapping closely with the pattern of TKS5. In contrast, ARHGAP17-
302 GFP appears later during the assembly phase (~1 min later than TKS5/wGBD in the example shown in
303 Fig. 7B), and it also shows a slight increase in signal intensity during invadopodia disassembly (Fig. 7 B
304 and Video 7). Quantitative analysis of intensity over time in multiple invadopodia confirmed this
305 observation (Fig. 7 C). Cross-correlation analysis between TKS5-mTagBFP2, ARHGAP17-GFP, and
306 dTomato-wGBD confirmed these observations, and showed that there is a positive correlation between
307 the three proteins, with the strongest correlation observed between Cdc42 activity and TKS5 (Fig. 7 D).
308 The analysis shows that the activity of Cdc42 occurred slightly earlier in time than TKS5. In contrast, the
309 correlation between ARHGAP17 and Cdc42 activity or TKS5 was weaker, most likely due to the ring
310 localization of ARHGAP17, with ARHGAP17 appearing later than both Cdc42 and TKS5. In addition, our
311 results also showed that in the absence of ARHGAP17 (ARHGAP17 KO) there was a significant increase in
312 the maximum Cdc42 activity at invadopodia when compared to CTRL or ARHGAP17 Rescue cells,
313 confirming that ARHGAP17 plays a role in the local regulation of Cdc42 at invadopodia (Fig. 7 F).

314 To characterize the spatiotemporal dynamics of ARHGAP17 and Cdc42 throughout the lifecycle of
315 invadopodia, we used the radial intensity analysis for each frame in time-lapse series of single
316 invadopodia co-expressing TKS5-mTagBFP2, ARHGAP17-GFP, and the wGBD Cdc42 localization sensor
317 (as in Fig. 7 B). A representative kymograph of several invadopodia averaged together is shown,
318 displaying the signal intensity over time for all the markers analyzed (x-axis, normalized to be
319 comparable), as well as the localization of the signal in relation to the center of the invadopodia (y-axis)
320 (Fig. 7 F). These results showed that Cdc42 activity (wGBD) was tightly localized at invadopodia,
321 specifically at the core throughout the lifetime of invadopodia. During the invadopodia assembly phase,
322 ARHGAP17 is recruited preferentially to the invadopodia ring as expected from our results from fixed
323 images in Fig. 4. Surprisingly, when the invadopodia starts to disassemble, the localization of ARHGAP17
324 shifts from the ring to the core, and this shift coincides with a decrease in Cdc42 signal at the core. This
325 change in localization can also be visualized as line profiles of selected time points from the time series
326 data (Fig. 7 G and H). At an early stage during invadopodia assembly (t 0.25), ARHGAP17 was found
327 predominantly in the ring (Fig. 7 G), while later during invadopodia disassembly (t 0.75), ARHGAP17 was
328 shifted to the core (Fig. 7 H). This shift of ARHGAP17 to the core is also associated with a decrease in the
329 peak intensity of both TKS5 and wGBD signal (Fig. 7 H) when compared to the peak intensity during
330 assembly (Fig. 7 G). When the kymograph analysis is repeated with the ΔC-ARHGAP17 mutant, which is
331 impaired in core localization, the shift to the invadopodia core at disassembly is completely lost (Fig. 7 I-
332 K). This shows that the shift in localization towards the core during disassembly is dependent on the C-
333 terminus of ARHGAP17. Taken together, these data suggest that ARHGAP17 at the ring restricts the
334 activity of Cdc42 to the core during invadopodia assembly and moves to the core later, where it
335 inactivates Cdc42 to promote invadopodia disassembly.

336 **An ARHGAP17/CIP4/Cdc42 complex regulates invadopodia**

337 We have shown that ARHGAP17 regulates Cdc42 at invadopodia in a RhoGAP-dependent manner.
338 However, we do not know what Cdc42 effector is downstream of this signaling pathway. A potential
339 candidate is Cdc42-interacting protein 4 (CIP4), a Cdc42 effector which has been previously shown to
340 interact with ARHGAP17 (Richnau and Aspenstrom, 2001). Furthermore, CIP4 also targets to
341 invadopodia and regulates their formation in breast cancer cells (Pichot et al., 2010). To validate these
342 observations in our model, we generated SUM159 cells stably expressing shRNA for CIP4 (Fig. 8 A) and
343 found that, as described previously (Pichot et al., 2010), there was a significant decrease in the
344 percentage of cells forming invadopodia when the expression of CIP4 was silenced (Fig. 8 B and C). We
345 then stained for endogenous CIP4 in PDBu-treated SUM159 cells and confirmed that CIP4 also targets
346 specifically to invadopodia in these cells (Fig. 8 D) and localizes predominantly to the invadopodia core
347 (Fig. 8 E). We also confirmed that ARHGAP17 binds CIP4 at endogenous levels using co-
348 immunoprecipitation (Fig. 8 F) and that the proline-rich region of ARHGAP17 is required for CIP4 binding
349 as was previously shown (Fig. 8 G) (Richnau and Aspenstrom, 2001). We next wanted to determine if
350 ARHGAP17 activity is coupled with CIP4 as part of a complex to regulate Cdc42 activity as has been
351 frequently observed with RhoGEFs and some RhoGAPs (Lawson and Ridley, 2018). Using GST-Cdc42
352 Q61L and CD ARHGAP17-GFP (which does not interact with Cdc42), we found that myc-CIP4 can bind to
353 active Cdc42 and CD ARHGAP17-GFP simultaneously (Fig. 8 G). These results suggest that
354 CIP/ARHGAP17/Cdc42 may form a complex in cells which could potentially coordinate the transition
355 between activation and inactivation of Cdc42.

356 We then wanted to characterize the roles of the ARHGAP17, CIP4, and Cdc42 activity in invadopodia.
357 When analyzing individual invadopodia expressing CIP4-GFP, TKS5-mTagBFP2, and dTomato-wGBD, we
358 found that CIP4 is present at invadopodia throughout their lifetime and overlaps closely with TKS5, both
359 spatially and temporally (Fig. 9 A and B and Video 8). Interestingly, Cdc42 activity, as determined by the
360 dTomato-wGBD biosensor, was present earlier in invadopodia lifetime than CIP4, while CIP4 was still
361 present in invadopodia after loss of Cdc42 activity (Fig. 9 A and B and Video 8). These temporal shifts
362 between CIP4 and Cdc42 activity were confirmed using cross-correlation analysis (Fig. 9 C). To determine
363 the role of the ARHGAP17-CIP4 interaction in the regulation of invadopodia, we investigated the
364 localization of ARHGAP17 (ARHGAP17-GFP expressed in ARHGAP17 KO cells) in CTRL cells compared to
365 cells overexpressing myc-CIP4. Interestingly, in cells overexpressing myc-CIP4, we observed a dramatic
366 shift from the typical ARHGAP17 localization enriched at the ring, to a predominantly core localization
367 (Fig. 9 D and E: top and middle panels). This was dependent on the interaction between ARHGAP17 and
368 CIP4 since the ΔC ARHGAP17-GFP mutant, which does not interact with CIP4, failed to relocate to the
369 core when co-expressed with myc-CIP4 (Fig. 9 D and E: bottom panels). Cross-correlation analysis of
370 invadopodia clusters confirmed these results, with a high cross-correlation coefficient between
371 ARHGAP17-GFP and myc-CIP4, which decreased drastically for the ΔC ARHGAP17-GFP and myc-CIP4 pair
372 (Fig. 9 F), even though both proteins still localized to invadopodia (Fig. 9 D; bottom panels). These
373 results suggest that the translocation of ARHGAP17 from the ring to the core observed upon initiation of
374 invadopodia disassembly depends on ARHGAP17's ability to bind to the core localized Cdc42 effector
375 CIP4.

376 Finally, we wanted to determine how the expression levels of ARHGAP17 and CIP4 influence each other
377 to regulate the invadopodia phenotype in SUM159 cells. To do this, we either silenced and/or
378 overexpressed CIP4 and ARHGAP17 in all possible combinations and quantified the percentage of cells

379 forming invadopodia after PDBu treatment. In agreement with what has been shown so far, our results
380 showed that ARHGAP17 and CIP4 have antagonistic roles at invadopodia; CIP4 overexpression increased
381 the number of cells with invadopodia while ARHGAP17 overexpression had an inhibitory effect. The
382 opposite is true for silencing their expression, with ARHGAP17 KO increasing and CIP4 KD decreasing the
383 number of cells with invadopodia (as shown in previous figures). When we tested combinations of
384 overexpressing and silencing ARHGAP17/CIP4, the function of one protein either synergized or
385 counteracted the effect of the other depending on the combination. If the two proteins were
386 simultaneously overexpressed or silenced, the phenotypic effects balanced each other out. For example,
387 the increase in invadopodia induced by CIP4 overexpression is restored to CTRL levels when ARHGAP17
388 is co-expressed. In contrast, a combination of silencing one gene and overexpressing the other worked
389 to exacerbate the phenotype. For example, ARHGAP17 KO with CIP4 overexpression showed higher
390 levels of invadopodia than either ARHGAP17 KO or CIP4-GFP overexpression alone (Fig. 9 G). Taken
391 together, our results suggest that the expression levels of ARHGAP17 and CIP4 help regulate the
392 equilibrium between invadopodia assembly and disassembly, and that CIP4 is key in recruiting
393 ARHGAP17 to core to inactivate Cdc42 and initiate invadopodia disassembly.

394 **Discussion**

395 Here, we have identified a novel role for ARHGAP17 in TNBC invadopodia dynamics by restricting the
396 activity of Cdc42 in time and space during invadopodia turnover. Our results demonstrate that the
397 function of ARHGAP17 is important throughout the invadopodia lifecycle. At early stages, during
398 invadopodia growth, ARHGAP17 localizes to the invadopodia ring, which helps to limit the activity of
399 Cdc42 to the actin core. Later, when invadopodia begin to disassemble, ARHGAP17 relocates to the
400 core, where it inactivates Cdc42 and promotes the disassembly of invadopodia. We also show that this
401 shift in localization is mediated by the interaction between ARHGAP17 and CIP4, a Cdc42 effector which
402 localizes to the core of invadopodia and is important for invadopodia assembly (Fig. 10). It should be
403 noted that, even in ARHGAP17 KO cells, invadopodia are still able to disassemble, and both the assembly
404 and disassembly rate remain unchanged. The fact that they still assemble and disassemble at a similar
405 rate may be indicative of redundancy in the system. ARHGAP17 has two closely related members of the
406 RhoGAP family, ARHGAP44 (RICH2) and SH3BP1, which may be compensating for the loss of ARHGAP17
407 (Aspenstrom, 2018). One way to explain the increased stability then, is that the events that trigger
408 disassembly, that is the recruitment of a Cdc42-GAP to the core, are either less frequent or delayed in
409 the absence of ARHGAP17, and the redundant function of SH3BP1 and/or ARHGAP44 cannot completely
410 compensate for this loss, and results in invadopodia remaining stable for a longer period. We plan to
411 examine the role of the three family members in future studies.

412 Our report is the first to describe ARHGAP17 at invadopodia and a direct mechanism regarding the link
413 between ARHGAP17 and cancer cell invasion. ARHGAP17 has been previously characterized as a tumor
414 suppressor and found to be downregulated in a variety of cancers, including colon, breast, and cervical,
415 where it functions to inhibit migration and invasion (Guo et al., 2019; Kiso et al., 2018; Pan et al., 2018;
416 Pan et al., 2022; Tian et al., 2022). ARHGAP17 is downregulated by VEGF/NRP1 signaling in TNBC which
417 was associated with increased Cdc42 activity, filopodia formation, and cell migration (Kiso et al., 2018).
418 ARHGAP17 expression was also found to inhibit invasion and metastasis of colon cancer in association
419 with decreased Wnt signaling (Pan et al., 2018), and in cervical cancer, ARHGAP17 suppressed cell
420 proliferation and tumor growth by inhibiting PI3K/AKT signaling (Guo et al., 2019). Our results suggest

421 that the tumor suppressor role of ARHGAP17 may depend in part in its ability to negatively regulate
422 invadopodia by inactivating Cdc42, leading to a decreased invasive capacity.

423 Cdc42 activity has long been recognized to be essential for both invadopodia and podosome formation,
424 regardless of the cell type or model system used (Ayala et al., 2009; Di Martino et al., 2014; Juin et al.,
425 2014; Moreau et al., 2003; Yamaguchi et al., 2005). Using our improved localization-based sensor, we
426 found that Cdc42 activity is present throughout the lifetime of invadopodia at the invadopodia core with
427 the strongest activity being present at the assembly phase and a decrease in activity being associated
428 with invadopodia disassembly. Cdc42 promotes the assembly of the actin core of invadopodia through
429 its effector N-WASP, which induces actin nucleating by activation of the Arp2/3 complex (Desmarais et
430 al., 2009; Juin et al., 2012; Juin et al., 2014; Lorenz et al., 2004; Monteiro et al., 2013; Yamaguchi et al.,
431 2005; Yu et al., 2012). N-WASP also binds to the SH3 domain of the invadopodia protein, TKS5 (Oikawa
432 et al., 2008). The link between Cdc42 and TKS5 is critical as Cdc42 activity and TKS5 are both essential
433 for invadopodia formation and function (Di Martino et al., 2014). Cdc42 activity also promotes
434 invadopodia function as marked by matrix degradation. Together with RhoA activity, Cdc42 has been
435 shown to promote ECM degradation through its interaction with the Cdc42 effector, IQGAP (Sakurai-
436 Yageta et al., 2008). Interactions between IQGAP and the exocyst protein complex control the delivery
437 of matrix metalloproteases to the membrane of invadopodia (Sakurai-Yageta et al., 2008). Inactivation
438 of Cdc42 at invadopodia by ARHGAP17 would then lead to the reduction of invadopodia formation and
439 activity by shutting down Cdc42-mediated actin nucleation and metalloprotease transport.

440 The activities of several Rho GTPases have been associated with invadopodia formation and function,
441 but very few have been studied at the level of detail shown in this manuscript. An exception is RhoC,
442 which in contrast to what we observed for Cdc42, is active at the ring and inactive at the core. This is
443 regulated by the combined action of the ring-localized p190 RhoGEF and the core localized p190RhoGAP
444 (Bravo-Cordero et al., 2011). Whether p190RhoGAP shifts from the core-to-the ring to inactivate at
445 RhoC is not clear from this study. However, like our study, it highlights the tight spatial and temporal
446 regulation of Rho GTPases, even within invadopodia subdomains.

447 We have not characterized the RhoGEF responsible for the activation of Cdc42 in our system. A potential
448 candidate is FGD1, which has been identified in previous reports as the RhoGEF that mediates the
449 activation of Cdc42 at both podosomes and invadopodia (Ayala et al., 2009; Daubon et al., 2011;
450 Zagryazhskaya-Masson et al., 2020). FGD1 localizes to invadopodia in metastatic melanoma and breast
451 cancer cells through its interaction with TKS5 and promotes the assembly of the actin core in a Cdc42-
452 dependent manner (Ayala et al., 2009; Zagryazhskaya-Masson et al., 2020). Another potential RhoGEF
453 candidate is Vav1, which has also been found to play a role in invadopodia formation in pancreatic
454 cancer cells by activating Cdc42 (Razidlo et al., 2014). In future studies, it will be interesting to
455 characterize the RhoGEF in the ARHGAP17/Cdc42/CIP4 pathway and the interplay between GEF and
456 GAP activity in regulating invadopodia dynamics.

457 Our study also shows that the Cdc42 effector CIP4 is important for the spatiotemporal regulation of
458 ARHGAP17 at invadopodia and may play a key role in coordinating the timing of Cdc42 inactivation, as it
459 can simultaneously interact with ARHGAP17 and Cdc42. We found that CIP4 localizes specifically to the
460 invadopodia core, and that its interaction with ARHGAP17 is required for the ring-to-core translocation
461 observed for ARHGAP17 at the initiation of invadopodia disassembly. CIP4 has previously been found to
462 localize at invadopodia and function as a positive regulator of invadopodia formation through activation

463 of N-WASP (Pichot et al., 2010). CIP4 seems to function as a scaffolding platform, as it can interact with
464 Cdc42, N-WASP, Src, and ARHGAP17 (Dombrosky-Ferlan et al., 2003; Pichot et al., 2010; Richnau and
465 Aspenstrom, 2001). CIP4 has two closely related family members which have also been shown to localize
466 to invadopodia and promote their formation: FBP17 (Formin Binding Protein 17) and Toca-1 (transducer
467 of Cdc42-dependent actin activity) (Chander et al., 2013; Suman et al., 2018; Yamamoto et al., 2011).
468 FBP17 and Toca-1 both interact with Cdc42 and N-WASP, promote the activation of N-WASP, and
469 stimulate actin nucleation through the Arp2/3 complex (Bu et al., 2010; Ho et al., 2004; Hu et al., 2011;
470 Takano et al., 2008; Tsujita et al., 2013; Tsujita et al., 2006). Considering that silencing CIP4 expression
471 does not completely abolish invadopodia formation, FBP17 and/or Toca-1 may compensate for CIP4 loss
472 in SUM159 cells.

473 CIP4, FBP17, and Toca-1 can all activate N-WASP and have been shown to link its activity to membrane
474 curvature sensing, membrane remodeling, and endocytosis through the F-BAR domains. (Chan Wah Hak
475 et al., 2018; Hartig et al., 2009; Takano et al., 2008; Tsujita et al., 2006). It is possible that CIP4 regulates
476 membrane curvature sensing and/or endocytosis at invadopodia, connecting these processes to actin
477 polymerization through N-WASP activation. Interestingly, ARHGAP17 also encodes a BAR domain at the
478 N-terminus, which is important for its targeting at invadopodia and may also play a role in curvature
479 sensing and membrane remodeling/trafficking. What the functional connection between the BAR
480 domains in CIP4 and ARHGAP17 remains to be determined.

481 It is not clear how the ring-to-core translocation is regulated, but phosphorylation is a possibility. Nagy
482 and colleagues have shown that ARHGAP17 is phosphorylated by PKA/PKG at S702, and that this
483 phosphorylation inhibits its binding to CIP4 (Nagy et al., 2015). It is possible then, that when targeted to
484 the ring, ARHGAP17 is phosphorylated, and a yet to be characterized stimulus triggers its
485 dephosphorylation at the initiation of disassembly, allowing it to bind to CIP4 and promoting the
486 translocation to the core and subsequent inactivation of Cdc42. Interestingly, CIP4 is also
487 phosphorylated by PKA at T225, and this phosphorylation appears to promote the formation of
488 invadopodia and enhance its interaction with Cdc42 (Tonucci et al., 2019). Future work will shed light in
489 the exact molecular mechanisms controlling the dynamics of ARHGAP17, Cdc42, and CIP4 in the
490 formation of invadopodia, the role of the activators (RhoGEFs), and their effect on actin polymerization
491 and other cellular functions.

492 Materials and Methods

493 Cell lines

494 HEK 293FT cells (Thermo Fisher Scientific) were used for all the pulldown experiments unless indicated
495 otherwise. The SUM159 cells were a gift from Carol Otey (UNC-Chapel Hill, NC). The HEK 293FT cells
496 were cultured in Dulbecco's modified Eagle's medium (DMEM) (GIBCO) containing 10% fetal bovine
497 serum (FBS) (Sigma-Aldrich), and antibiotics (penicillin-streptomycin) (Corning). The SUM159 cells were
498 cultured in Ham's F12 (Cytiva) with 10% FBS, 5 µg/ml insulin (GIBCO), 1 µg/ml hydrocortisone (Sigma-
499 Aldrich), and antibiotics. All cell lines were grown at 37 °C and 5% CO^2. Mycoplasma was tested regularly
500 by staining with Hoechst 33342 (AnaSpec Inc.).

501 Reagents and antibodies

502 Antibodies against the following proteins were used: ARHGAP17 (Custom antibody, antigen sequence:
503 EPHRSIFPEMHSDSASKDVPGR, Pacific Immunology); cortactin (sc-11408) (Santa Cruz); myc (13-2500)
504 (Invitrogen); tubulin (T9028) and vinculin (V9131) (Sigma-Aldrich); CIP4 (612556), paxillin (610051),
505 Cdc42 (610929), and Rac1 (610650) (BD Biosciences). F-actin was stained with Alexa Fluor-405, -488, -
506 594, -647, and -750 conjugated to phalloidin (Thermo Fisher Scientific). For immunofluorescence, the
507 following secondary antibodies were used: Alexa Fluor-488, -568, -594, -647-conjugated anti-mouse-IgG
508 and anti-rabbit-IgG secondary antibodies (A32723, A32731, A11004, A11011, A11032, A11037, A21236,
509 A21245; Thermo Fisher Scientific). For western blot analysis the following secondary antibodies were
510 used: horseradish peroxidase (HRP)conjugated anti-mouse-IgG and anti-rabbit-IgG (715-035-151 and
511 711-035-152; Jackson Immunoresearch). Phorbol-12,13-dibutyrate (PDBu) (P1269) was from Sigma-
512 Aldrich.

513 **DNA constructs**

514 Constructs generated for this study: pCMV-myc-ARHGAP17, pLenti-myc-ARHGAP17, pCI-CD-ARHGAP17-
515 GFP, pC1-CMVdel-dTomato-1x-wGBD, pEGFP-ΔBAR-ARHGAP17, pLenti-BAR-ARHGAP17-GFP, pLenti-ΔC-
516 ARHGAP17-GFP, pDG462-ARHGAP17-KO constructs were generated using the pDG462 backbone
517 (Adikusuma et al., 2017) (exon 1 targets: CAGCTGGCTAACCAGACCG and GTTGAACTGCTTCTTCATGG;
518 exon 3 targets: AGCATGGCACCGATGCCGAG and CCAAGCGCTTATGGGAATGG).

519 Previously published or purchased constructs: pAd-CMV-mCherry-Cortactin (Goicoechea et al., 2017);
520 H2A-mTq2, H2A-mTq2-RhoA-G14V-ΔCAAX, H2A-mTq2-Rac1-G12V-ΔCAAX, and H2A-mTq2-Cdc42-G12V-
521 ΔCAAX, pC1-CMVdel-dTomato (Mahlandt et al., 2021); pCMV6-myc-Trip10 (OriGene-MR208703); All
522 shRNA were from the RNAi Consortium shRNA Library, purchased through Sigma-Aldrich (Table 1).

523 Constructs received as a gift: pCI-C-EGFP-Rich1 and pCI-C-EGFP-CIP4 (Harvey T. McMahon, MRC
524 Laboratory of Molecular biology); pLV-mNeonGreen-CAAX and pLV-Scarlet-CAAX (Jaap van Buul,
525 Sanquin); pmTagBFP2-N1-TKS5 and pmScarlet-N1-TKS5 (Lou Hodgson, Albert Einstein College of
526 Medicine); pDG462 (Paul Thomas, Addgene plasmid # 100903); pFUGW-UbC-1T17 (Yi Wu, UConn
527 Health, Farmington, CT) (Reinhard et al., 2017).

528 **Table 1. shRNAs used in this study**

#	Protein Name	Gene Symbol	Reference Sequence	OligoID-1	OligoID-2	OligoID-3	OligoID-4	OligoID-5
1	CDGAP	CDGAP	NM_020754	TRCN0000047638	TRCN0000047639	TRCN0000047640	TRCN0000047641	TRCN0000047642
2	Chimerin1	CHN1	NM_001025201	TRCN0000047798	TRCN0000047799	TRCN0000047800	TRCN0000047801	TRCN0000047802
3	Chimerin2	CHN2	NM_001039936	TRCN0000047738	TRCN0000047739	TRCN0000047740	TRCN0000047741	TRCN0000047742
4	CIP4	TRIP10	NM_001288962.2	TRCN0000063184	TRCN0000063185	TRCN0000063186	TRCN0000063187	NA
5	DLC-1	DLC1	NM_001164271	TRCN0000047823	TRCN0000047824	TRCN0000047825	TRCN0000047826	TRCN0000047827
6	FilGAP	ARHGAP24	NM_001025616	TRCN0000048303	TRCN0000048304	TRCN0000048305	TRCN0000048306	TRCN0000048307
7	GMIP	GMIP	NM_016573	TRCN0000007093	TRCN0000007094	TRCN0000007095	TRCN0000007096	NA
8	GRAF1	GRAF	NM_001135608	TRCN0000029754	TRCN0000029755	TRCN0000029756	TRCN0000029757	TRCN0000029758

9	GRAF2	ARHGAP10	NM_024605	TRCN0000048473	TRCN0000048474	TRCN0000048475	TRCN0000048476	TRCN0000048477
10	GRIT	RICS	NM_001142685	TRCN0000048358	TRCN0000048359	TRCN0000048360	TRCN0000048361	TRCN0000048362
11	Myosin-IXB	MYO9B	NM_001130065	TRCN0000007137	TRCN0000007138	TRCN0000007139	TRCN0000007140	TRCN0000007141
12	Non-targeting	Non-targeting	NA	RHS4459	NA	NA	NA	NA
13	p190-A	GRLF1	NM_004491	TRCN0000022184	TRCN0000022185	TRCN0000022186	TRCN0000022187	TRCN0000022188
14	p190-B	ARHGAP5	NM_001030055	TRCN0000006475	TRCN0000006476	TRCN0000006477	TRCN0000006479	TRCN0000012703
15	RhoGAP1	ARHGAP1	NM_004308	TRCN0000047298	TRCN0000047299	TRCN0000047300	TRCN0000047301	TRCN0000047302
16	RhoGAP12	ARHGAP12	NM_018287	TRCN0000047263	TRCN0000047264	TRCN0000047265	TRCN0000047266	TRCN0000047267
17	RICH1	ARHGAP17	NM_001006634	TRCN0000047448	TRCN0000047449	TRCN0000047450	TRCN0000047451	TRCN0000047452
18	SRGAP1	SRGAP1	NM_020762	TRCN0000047553	TRCN0000047554	TRCN0000047555	TRCN0000047556	TRCN0000047557
19	SRGAP2	SRGAP2	NM_001042758	TRCN0000047958	TRCN0000047959	TRCN0000047960	TRCN0000047962	TRCN0000166364
20	SRGAP3	SRGAP3	NM_001033117	TRCN0000047563	TRCN0000047564	TRCN0000047565	TRCN0000047566	TRCN0000047567
21	TCGAP	SNX26	NM_001172630	TRCN0000151287	TRCN0000152300	TRCN0000153966	TRCN0000154588	TRCN0000156215

529

530 **Cell lysis and immunoblotting**

531 Cells cultured on 100 mm tissue culture dishes were rinsed with TBS and 1 mM $MgCl_2$ and then scraped
532 into a lysis buffer containing 50 mM Tris-HCl pH 7.4, 10 mM MgCl2, 150 mM NaCl, 1% Triton X-100, and
533 EZBlock protease inhibitor cocktail (BioVision). The supernatant was collected after centrifugation at
534 16,800g for 10 min. For immunoblotting, lysates were boiled in 2× Laemmli buffer, and were resolved by
535 SDS-PAGE. The proteins were transferred onto PVDF and immunoblotted with the indicated antibodies.
536 Immunocomplexes were visualized using the Immobilon Western Millipore Chemiluminescence HRP
537 substrate (Millipore).

538 **Rho GTPase activity assay**

539 Active Cdc42 pulldown experiments were performed as described previously (Goicoechea et al., 2014).
540 Briefly, SUM159 cells were lysed in 50 mM Tris-HCl pH 7.4, 10 mM MgCl2, 150 mM NaCl, 1% Triton X-
541 100, and EZBlock protease inhibitor cocktail. After clearing the lysates by centrifugation at 14,000 g for 5
542 min, the protein concentrations of the supernatants were determined, and equal amounts of total
543 protein were incubated with 50 µg of GST–PBD, and rotated for 30 min at 4 °C. Subsequently the beads
544 were washed three times in lysis buffer. Pull-downs and lysates were then immunoblotted for Cdc42.

545 **Immunofluorescence**

546 For TIRF experiments, cells were grown in 8-well 1.5 glass bottom µ-slides (Ibidi), otherwise, cells were
547 grown on 1.5 glass coverslips (Thermo Fisher Scientific). For immunofluorescence, cells were fixed for 10
548 min with 4% paraformaldehyde and quenched with 10 mM ammonium chloride. Cells were then

549 permeabilized with 0.1% Triton X-100 in PBS for 7 min. The coverslips were then washed with PBS and
550 blocked with PBS/2.5% goat serum/0.2% Tween 20 for 5 min, followed by 5 min of blocking with
551 PBS/0.4% fish skin gelatin/0.2% Tween 20. Cells then were incubated with the primary antibody for 1 h
552 at room temperature. Coverslips were washed 5 times with PBS/0.2% Tween 20 followed by 5 min of
553 blocking with PBS/0.4% fish skin gelatin/0.2% Tween 20 and 5 min with PBS/2.5% goat serum/0.2%
554 Tween 20. Secondary antibody diluted in the blocking solution was then added for 45 min, washed 5
555 times with PBS/0.2% Tween, and mounted on glass slides in Mowiol mounting solution (Electron
556 Microscopy Sciences). For TIRF experiments, the cells were washed twice with PBS to remove any
557 detergent and kept in PBS for imaging.

558 **STORM microscopy**

559 For the STORM immunofluorescence, cells were fixed for 10 min with 4% paraformaldehyde and
560 quenched with 10 mM ammonium chloride in 35 mm glass-bottomed dishes (81158, Ibidi). Cells were
561 then permeabilized with 0.1% Triton X-100 in PBS for 7 min. The samples were then washed with PBS
562 and blocked with PBS/2.5% goat serum/0.2% Tween 20 for 10 min, followed by 10 min of blocking with
563 PBS/0.4% fish skin gelatin/0.2% Tween 20. Cells then were incubated with the primary antibody for 1 h
564 at room temperature. Samples were washed 5 times with PBS/0.2% Tween 20 (2 times for 5 min and 3
565 times for 10 min) followed by 10 min of blocking with PBS/0.4% fish skin gelatin/0.2% Tween 20 and 10
566 min with PBS/2.5% goat serum/0.2% Tween 20. Secondary antibody (Alexa Fluor 488 and 647) diluted in
567 the blocking solution was then added for 45 min, washed 5 times with PBS/0.2% Tween as before, and
568 then washed twice with PBS to remove any detergent. Samples were imaged in OxEA buffer (Nahidiazar
569 et al., 2016) for 10,000 frames at 100 Hz for each channel starting with the longer wavelength
570 fluorophore first. The minimal light intensity to sufficiently send the fluorophores to the dark state was
571 used to limit bleaching (Diekmann et al., 2020). Reconstruction of STORM data was performed using
572 Nikon NIS-Elements AR software.

573 **FRET acquisition and processing**

574 To monitor changes in Cdc42 activity in live cells we used a previously characterized dimerization-
575 optimized reporter for activation (DORA) single chain Cdc42 biosensor (generous gift from Yi Wu, UConn
576 Health, Farmington, CT) (Reinhard et al., 2017). Experiments were carried out as previously described for
577 a similar Rac sensor (Baker et al., 2020; Cooke et al., 2021). Briefly, SUM159 cells stably expressing low
578 levels of the FRET-sensor together with a marker for invadopodia (mCherry-cortactin), were treated with
579 PDBu to induce invadopodia. We used 1:100 Oxyfluor reagent (Oxyrase Inc.) and 10 mM DL-lactate
580 (Sigma-Aldrich) to reduce oxygen free radicals. Cells were imaged every 15 s with 2 x 2 binning and 16-
581 bit depth, using a Nikon Eclipse Ti2 microscope equipped for FRET imaging (see Microscopes). Raw
582 images were processed in batch using a custom designed macro in ImageJ, which included corrections to
583 account for background and bleaching, and a median filter with a 1-pixel radius was applied to reduce
584 noise artifacts. The FRET ratio was calculated, and a 16-color LUT was applied to allow for the
585 visualization of Cdc42 activation.

586 **Microscopes**

587 For STORM, TIRF, and live imaging experiments, a Nikon Eclipse Ti2 microscope was used equipped with
588 a Tokai Hit STX stage top incubator, Apo TIRF 60x NA 1.49 oil immersion and SR HP Apo TIRF 100x NA
589 1.49 oil immersion objectives, Hamamatsu ORCA-Flash 4.0 camera, Princeton Instruments ProEM back-

590 illuminated EMCCD camera, Lumencor SPECTRA X solid-state light source, Agilent laser unit (405-, 488-,
591 561-, and 647-nm), and NIS-Elements AR software. The microscope is equipped with a dichroic splitter
592 to facilitate simultaneous acquisition of Cerulean3 and Venus emissions.

593 Confocal data was collected using a Leica Stellaris 5 laser scanning confocal equipped with an HC PL APO
594 63x/1.40 OIL CS2 objective and LAS X software, or an Andor Dragonfly 200 spinning disk confocal on a
595 Leica DMI8 platform equipped with an HC PL FLUOTAR L 20X air objective, HC PL APO 63x/1.40 oil
596 objective, Zyla4 camera, and Fusion software.

597 Brightfield images were acquired on an Olympus IX81 inverted microscope equipped with a UPlanFL N
598 10×/0.30 Ph1 air objective, Hamamatsu ORCA-Flash 4.0 camera, and cellSens software.

599 **Matrix degradation assay**

600 The matrix degradation assay was modified from the Weed lab protocol (Martin et al., 2012). In brief,
601 glass coverslips were coated with polylysine (50 µg/mL in water) and incubated for 20 minutes at room
602 temperature and washed 3x with PBS. The coverslips were then fixed with ice-cold 0.5% glutaraldehyde
603 in PBS and incubated on ice for 15 minutes and washed 3x with ice-cold PBS. The last wash was
604 completely removed, and the coverslips were coated with a 37 °C solution consisting of 6 parts 1%
605 (w/w) stock gelatin/sucrose solution in PBS, 1 part of Oregon Green 488-conjugated gelatin (Thermo
606 Fisher Scientific), and 2 parts collagen IV (500 µg/mL stock). The excess matrix solution was aspirated off
607 and incubated for 10 min at room temperature in the dark. The coverslips were then washed 3x with
608 PBS and quenched with NaBH4 (5 mg/ml in PBS) for 15 min. The coverslips were washed 3x with PBS
609 and sterilized with 70% ethanol for 30 min at room temperature. Finally, the coverslips were washed 3x
610 with sterile PBS and stored at 4 °C for up to two weeks before use.

611 For the assay, SUM159 cells were plated on the gelatin coverslips and treated with PDBu for 24 hours.
612 The coverslips were then fixed, stained with AlexaFluor-594 Phalloidin, and mounted using the
613 described immunofluorescence protocol. For each condition, 20 random fields-of-view (FOV) were
614 acquired via spinning disk confocal. Degradation was quantified by dividing the area of degradation for
615 each image by the total cell area and normalizing the results to the CTRL cells.

616 **Invasion assays**

617 The spheroid invasion assay was performed using the previously described method (Vinci et al., 2015). In
618 brief, 4,000 cells were transferred into ultra-low attachment (ULA) 96-well round bottom plate in 200 µL
619 of media and grown for 4 days. Once the spheroids had matured, 100 µL of media was removed and 100
620 µL of Matrigel (354230, Corning) was added and allowed to polymerase at 37 °C for 1 hr. After
621 polymerization, 100 µL of media were added on top of the Matrigel. The spheroids were imaged every
622 24 hr for 72 hr. For measuring spheroid proliferation, the same process was followed except the
623 Matrigel was omitted.

624 The inverse invasion assay was modified from previous methods (Goswami et al., 2005; Scott et al.,
625 2011). SUM159 cells stably expressing mNeon-CAAX were plated in a CELLview glass bottom 10-well
626 slide (Greiner Bio-One) to achieve 100% confluency overnight. The cells were then washed 3 times with
627 PBS to remove growth factors and media. 100 µL of 50% Matrigel in serum free media was added to
628 each of the wells. The cells were then incubated at 37 °C for 30 min to polymerize the matrix. 100 µL
629 serum containing media was added to each well. The cells were then incubated overnight and at least 3

random regions per well were imaged with spinning disk confocal equipped with a long working distance 20X objective.

Radial intensity analysis

Invadopodia radial intensity measurements were performed in ImageJ using a custom macro and the calculations were performed with RStudio. Briefly, a 3 µm line ROI was drawn across the center of a single invadopodia based on the F-actin channel. Then the pixel intensity was measured across the ROI after which the ROI was rotated 3 degrees. This was repeated until the ROI completed a complete revolution and was then repeated for each channel of the image. For each invadopodia measured, the intensity values were averaged together to calculate the average intensity radiating out from the center of the invadopodia. The intensity measurements can then be plotted directly or used to calculate the distance of the peak signal from the center of each invadopodia or the relative signal intensity for each invadopodia by dividing the average signal intensity within 1 µm from the center of the invadopodia by the signal 1.5 µm from the invadopodia center.

Invadopodia dynamics analysis

The invadopodia dynamics measurements were performed in ImageJ using a custom macro and the calculations were performed with RStudio. Briefly, the center of a random, single invadopodia that forms and disassembles within the duration of the video was identified for each frame. Then, for each frame, a 1 µm diameter circle was drawn around the invadopodia and a 1 µm band was drawn around the circle. The average intensity within the circle was then divided by the average intensity within the band to calculate the relative signal intensity at the invadopodia for each frame. The quantification of the dynamics was performed as previously described for cell ruffle dynamics (Kreider-Letterman et al., 2022b).

Statistical analysis

Values calculated from at least three independent experiments were compared by an unpaired student's t-test using GraphPad Prism or RStudio unless otherwise indicated. Otherwise, a one-way ANOVA analysis followed by a Tukey's test was performed. Technical replicates are defined in this study as individual cells or invadopodia while biological replicates are defined as the averages of technical replicates or cell populations from independently prepared samples. Biological replicates were assumed to have normal distribution (Fay and Gerow, 2013). $P<0.05$ was considered statistically significant. Error bars represent the S.E.M. unless otherwise indicated.

Acknowledgements

The authors would like to thank Carol Otey, Harvey T. McMahon, Jaap van Buul, and Lou Hodgson for providing reagents. We would also like to thank Jaap van Buul, Jose J. Bravo-Cordero, Marcelo Kazanietz, as well as the members of the Garcia-Mata and Goedhart lab for critical comments and valuable discussion. This work was supported by a Nederlandse Organisatie voor Wetenschappelijk Onderzoek ALW-OPEN grant (ALWOP.306) (to E.K.M.) and 1R15CA199101, R03CA234693, and R01-GM136826-01 grants from the NIH (to R.G.-M.).

Competing interests

668 The authors declare no competing interests.

669 ## References

670 Adikusuma, F., C. Pfitzner, and P.Q. Thomas. 2017. Versatile single-step-assembly CRISPR/Cas9 vectors
671 for dual gRNA expression. *PLoS One*. 12:e0187236.
672 Al Haddad, M., R. El-Rif, S. Hanna, L. Jaafar, R. Dennaoui, S. Abdellatef, V. Miskolci, D. Cox, L. Hodgson,
673 and M. El-Sibai. 2020. Differential regulation of rho GTPases during lung adenocarcinoma
674 migration and invasion reveals a novel role of the tumor suppressor StarD13 in invadopodia
675 regulation. *Cell Commun Signal*. 18:144.
676 Artym, V.V., Y. Zhang, F. Seillier-Moiseiwitsch, K.M. Yamada, and S.C. Mueller. 2006. Dynamic
677 interactions of cortactin and membrane type 1 matrix metalloproteinase at invadopodia:
678 defining the stages of invadopodia formation and function. *Cancer Res*. 66:3034-3043.
679 Aspenstrom, P. 2018. BAR Domain Proteins Regulate Rho GTPase Signaling. *Adv Exp Med Biol*.
680 Ayala, I., G. Giacchetti, G. Caldieri, F. Attanasio, S. Mariggio, S. Tete, R. Polishchuk, V. Castronovo, and R.
681 Buccione. 2009. Faciogenital dysplasia protein Fgd1 regulates invadopodia biogenesis and
682 extracellular matrix degradation and is up-regulated in prostate and breast cancer. *Cancer Res*.
683 69:747-752.
684 Badowski, C., G. Pawlak, A. Grichine, A. Chabadel, C. Oddou, P. Jurdic, M. Pfaff, C. Albigès-Rizo, and M.R.
685 Block. 2008. Paxillin phosphorylation controls invadopodia/podosomes spatiotemporal
686 organization. *Mol Biol Cell*. 19:633-645.
687 Baker, M.J., M. Cooke, G. Kreider-Letterman, R. Garcia-Mata, P.A. Janmey, and M.G. Kazanietz. 2020.
688 Evaluation of active Rac1 levels in cancer cells: a case of misleading conclusions from
689 immunofluorescence analysis. *Journal of Biological Chemistry*.
690 Benink, H.A., and W.M. Bement. 2005. Concentric zones of active RhoA and Cdc42 around single cell
691 wounds. *J Cell Biol*. 168:429-439.
692 Berginski, M.E., E.A. Vitriol, K.M. Hahn, and S.M. Gomez. 2011. High-resolution quantification of focal
693 adhesion spatiotemporal dynamics in living cells. *PLoS One*. 6:e22025.
694 Branch, K.M., D. Hoshino, and A.M. Weaver. 2012. Adhesion rings surround invadopodia and promote
695 maturation. *Biol Open*. 1:711-722.
696 Bravo-Cordero, J.J., M. Oser, X. Chen, R. Eddy, L. Hodgson, and J. Condeelis. 2011. A novel
697 spatiotemporal RhoC activation pathway locally regulates cofilin activity at invadopodia. *Curr*
698 *Biol*. 21:635-644.
699 Bu, W., K.B. Lim, Y.H. Yu, A.M. Chou, T. Sudhaharan, and S. Ahmed. 2010. Cdc42 interaction with N-
700 WASP and Toca-1 regulates membrane tubulation, vesicle formation and vesicle motility:
701 implications for endocytosis. *PLoS One*. 5:e12153.
702 Chan Wah Hak, L., S. Khan, I. Di Meglio, A.L. Law, S. Lucken-Ardjomande Hasler, L.M. Quintaneiro, A.P.A.
703 Ferreira, M. Krause, H.T. McMahon, and E. Boucrot. 2018. FBP17 and CIP4 recruit SHIP2 and
704 lamellipodin to prime the plasma membrane for fast endophilin-mediated endocytosis. *Nat Cell*
705 *Biol*. 20:1023-1031.
706 Chander, H., P. Truesdell, J. Meens, and A.W. Craig. 2013. Transducer of Cdc42-dependent actin
707 assembly promotes breast cancer invasion and metastasis. *Oncogene*. 32:3080-3090.
708 Cooke, M., G. Kreider-Letterman, M.J. Baker, S. Zhang, N.T. Sullivan, E. Eruslanov, M.C. Abba, S.M.
709 Goicoechea, R. García-Mata, and M.G. Kazanietz. 2021. FARP1, ARHGEF39, and TIAM2 are
710 essential receptor tyrosine kinase effectors for Rac1-dependent cell motility in human lung
711 adenocarcinoma. *Cell Rep*. 37:109905.

712 Daubon, T., R. Buccione, and E. Génot. 2011. The Aarskog-Scott syndrome protein Fgd1 regulates
713 podosome formation and extracellular matrix remodeling in transforming growth factor β-
714 stimulated aortic endothelial cells. *Mol Cell Biol*. 31:4430-4441.
715 Desmarais, V., H. Yamaguchi, M. Oser, L. Soon, G. Mouneimne, C. Sarmiento, R. Eddy, and J. Condeelis.
716 2009. N-WASP and cortactin are involved in invadopodium-dependent chemotaxis to EGF in
717 breast tumor cells. *Cell Motil Cytoskeleton*. 66:303-316.
718 Di Martino, J., L. Paysan, C. Gest, V. Lagrée, A. Juin, F. Saltel, and V. Moreau. 2014. Cdc42 and Tks5: a
719 minimal and universal molecular signature for functional invadosomes. *Cell Adh Migr*. 8:280-
720 292.
721 Diekmann, R., M. Kahnwald, A. Schoenit, J. Deschamps, U. Matti, and J. Ries. 2020. Optimizing imaging
722 speed and excitation intensity for single-molecule localization microscopy. *Nat Methods*.
723 17:909-912.
724 Diring, J., S. Mouilleron, N.Q. McDonald, and R. Treisman. 2019. RPEL-family rhoGAPs link Rac/Cdc42
725 GTP loading to G-actin availability. *Nat Cell Biol*. 21:845-855.
726 Dombrosky-Ferlan, P., A. Grishin, R.J. Botelho, M. Sampson, L. Wang, W.A. Rudert, S. Grinstein, and S.J.
727 Corey. 2003. Felic (CIP4b), a novel binding partner with the Src kinase Lyn and Cdc42, localizes to
728 the phagocytic cup. *Blood*. 101:2804-2809.
729 Fay, D.S., and K. Gerow. 2013. A biologist's guide to statistical thinking and analysis. *WormBook*:1-54.
730 García-Mata, R., K. Wennerberg, W.T. Arthur, N.K. Noren, S.M. Ellerbroek, and K. Burridge. 2006.
731 Analysis of activated GAPs and GEFs in cell lysates. *Methods Enzymol*. 406:425-437.
732 Gligorijevic, B., A. Bergman, and J. Condeelis. 2014. Multiparametric classification links tumor
733 microenvironments with tumor cell phenotype. *PLoS Biol*. 12:e1001995.
734 Goicoechea, S.M., B. Bednarski, R. Garcia-Mata, H. Prentice-Dunn, H.J. Kim, and C.A. Otey. 2009. Palladin
735 contributes to invasive motility in human breast cancer cells. *Oncogene*. 28:587-598.
736 Goicoechea, S.M., R. García-Mata, J. Staub, A. Valdivia, L. Sharek, C.G. McCulloch, R.F. Hwang, R. Urrutia,
737 J.J. Yeh, H.J. Kim, and C.A. Otey. 2014. Palladin promotes invasion of pancreatic cancer cells by
738 enhancing invadopodia formation in cancer-associated fibroblasts. *Oncogene*. 33:1265-1273.
739 Goicoechea, S.M., A. Zinn, S.S. Awadia, K. Snyder, and R. Garcia-Mata. 2017. A RhoG-mediated signaling
740 pathway that modulates invadopodia dynamics in breast cancer cells. *J Cell Sci*. 130:1064-1077.
741 Goswami, S., E. Sahai, J.B. Wyckoff, M. Cammer, D. Cox, F.J. Pixley, E.R. Stanley, J.E. Segall, and J.S.
742 Condeelis. 2005. Macrophages promote the invasion of breast carcinoma cells via a colony-
743 stimulating factor-1/epidermal growth factor paracrine loop. *Cancer Res*. 65:5278-5283.
744 Guo, Q., Y. Xiong, Y. Song, K. Hua, and S. Gao. 2019. ARHGAP17 suppresses tumor progression and up-
745 regulates P21 and P27 expression via inhibiting PI3K/AKT signaling pathway in cervical cancer.
746 *Gene*. 692:9-16.
747 Harada, A., B. Furuta, K. Takeuchi, M. Itakura, M. Takahashi, and M. Umeda. 2000. Nadrin, a novel
748 neuron-specific GTPase-activating protein involved in regulated exocytosis. *J Biol Chem*.
749 275:36885-36891.
750 Hartig, S.M., S. Ishikura, R.S. Hicklen, Y. Feng, E.G. Blanchard, K.A. Voelker, C.S. Pichot, R.W. Grange, R.M.
751 Raphael, A. Klip, and S.J. Corey. 2009. The F-BAR protein CIP4 promotes GLUT4 endocytosis
752 through bidirectional interactions with N-WASp and Dynamin-2. *J Cell Sci*. 122:2283-2291.
753 Ho, H.Y., R. Rohatgi, A.M. Lebensohn, M. Le, J. Li, S.P. Gygi, and M.W. Kirschner. 2004. Toca-1 mediates
754 Cdc42-dependent actin nucleation by activating the N-WASP-WIP complex. *Cell*. 118:203-216.
755 Hoshino, D., K.M. Branch, and A.M. Weaver. 2013. Signaling inputs to invadopodia and podosomes. *J*
756 *Cell Sci*. 126:2979-2989.
757 Hoshino, D., J. Jourquin, S.W. Emmons, T. Miller, M. Goldgof, K. Costello, D.R. Tyson, B. Brown, Y. Lu,
758 N.K. Prasad, B. Zhang, G.B. Mills, W.G. Yarbrough, V. Quaranta, M. Seiki, and A.M. Weaver. 2012.

759 Network analysis of the focal adhesion to invadopodia transition identifies a PI3K-PKCα invasive
760 signaling axis. *Sci Signal*. 5:ra66.
761 Hu, J., A. Mukhopadhyay, and A.W. Craig. 2011. Transducer of Cdc42-dependent actin assembly
762 promotes epidermal growth factor-induced cell motility and invasiveness. *J Biol Chem*.
763 286:2261-2272.
764 Juin, A., C. Billottet, V. Moreau, O. Destaing, C. Albiges-Rizo, J. Rosenbaum, E. Genot, and F. Saltel. 2012.
765 Physiological type I collagen organization induces the formation of a novel class of linear
766 invadosomes. *Mol Biol Cell*. 23:297-309.
767 Juin, A., J. Di Martino, B. Leitinger, E. Henriet, A.S. Gary, L. Paysan, J. Bomo, G. Baffet, C. Gauthier-
768 Rouvière, J. Rosenbaum, V. Moreau, and F. Saltel. 2014. Discoidin domain receptor 1 controls
769 linear invadosome formation via a Cdc42-Tuba pathway. *J Cell Biol*. 207:517-533.
770 Kedziora, K.M., D. Leyton-Puig, E. Argenzio, A.J. Boumeester, B. van Butselaar, T. Yin, Y.I. Wu, F.N. van
771 Leeuwen, M. Innocenti, K. Jalink, and W.H. Moolenaar. 2016. Rapid Remodeling of Invadosomes
772 by Gi-coupled Receptors: DISSECTING THE ROLE OF Rho GTPases. *J Biol Chem*. 291:4323-4333.
773 Kim, S.H., Z. Li, and D.B. Sacks. 2000. E-cadherin-mediated cell-cell attachment activates Cdc42. *J Biol*
774 *Chem*. 275:36999-37005.
775 Kiso, M., S. Tanaka, S. Saji, M. Toi, and F. Sato. 2018. Long isoform of VEGF stimulates cell migration of
776 breast cancer by filopodia formation via NRP1/ARHGAP17/Cdc42 regulatory network. *Int J*
777 *Cancer*.
778 Kreider-Letterman, G., N.M. Carr, and R. Garcia-Mata. 2022a. Fixing the GAP: The role of RhoGAPs in
779 cancer. *Eur J Cell Biol*. 101:151209.
780 Kreider-Letterman, G., M. Cooke, S.M. Goicoechea, M.G. Kazanietz, and R. Garcia-Mata. 2022b.
781 Quantification of ruffle area and dynamics in live or fixed lung adenocarcinoma cells. *STAR*
782 *Protocols*. 3:101437.
783 Lawson, C.D., and A.J. Ridley. 2018. Rho GTPase signaling complexes in cell migration and invasion. *J Cell*
784 *Biol*. 217:447-457.
785 Lorenz, M., H. Yamaguchi, Y. Wang, R.H. Singer, and J. Condeelis. 2004. Imaging sites of N-wasp activity
786 in lamellipodia and invadopodia of carcinoma cells. *Curr Biol*. 14:697-703.
787 Machacek, M., L. Hodgson, C. Welch, H. Elliott, O. Pertz, P. Nalbant, A. Abell, G.L. Johnson, K.M. Hahn,
788 and G. Danuser. 2009. Coordination of Rho GTPase activities during cell protrusion. *Nature*.
789 461:99-103.
790 Mahlandt, E.K., J.J.G. Arts, W.J. van der Meer, F.H. van der Linden, S. Tol, J.D. van Buul, T.W.J. Gadella,
791 and J. Goedhart. 2021. Visualizing endogenous Rho activity with an improved localization-based,
792 genetically encoded biosensor. *J Cell Sci*. 134.
793 Martin, K.H., K.E. Hayes, E.L. Walk, A.G. Ammer, S.M. Markwell, and S.A. Weed. 2012. Quantitative
794 measurement of invadopodia-mediated extracellular matrix proteolysis in single and
795 multicellular contexts. *J Vis Exp*:e4119.
796 Meirson, T., A. Genna, N. Lukic, T. Makhnii, J. Alter, V.P. Sharma, Y. Wang, A.O. Samson, J.S. Condeelis,
797 and H. Gil-Henn. 2018. Targeting invadopodia-mediated breast cancer metastasis by using ABL
798 kinase inhibitors. *Oncotarget*. 9:22158-22183.
799 Monteiro, P., C. Rossé, A. Castro-Castro, M. Irondelle, E. Lagoutte, P. Paul-Gilloteaux, C. Desnos, E.
800 Formstecher, F. Darchen, D. Perrais, A. Gautreau, M. Hertzog, and P. Chavrier. 2013. Endosomal
801 WASH and exocyst complexes control exocytosis of MT1-MMP at invadopodia. *J Cell Biol*.
802 203:1063-1079.
803 Moreau, V., F. Tatin, C. Varon, and E. Génot. 2003. Actin can reorganize into podosomes in aortic
804 endothelial cells, a process controlled by Cdc42 and RhoA. *Mol Cell Biol*. 23:6809-6822.
805 Moshfegh, Y., J.J. Bravo-Cordero, V. Miskolci, J. Condeelis, and L. Hodgson. 2014. A Trio-Rac1-Pak1
806 signalling axis drives invadopodia disassembly. *Nat Cell Biol*. 16:574-586.

807 Murphy, D.A., and S.A. Courtneidge. 2011. The 'ins' and 'outs' of podosomes and invadopodia:
808 characteristics, formation and function. *Nat Rev Mol Cell Biol*. 12:413-426.
809 Nagy, Z., K. Wynne, A. von Kriegsheim, S. Gambaryan, and A. Smolenski. 2015. Cyclic Nucleotide-
810 dependent Protein Kinases Target ARHGAP17 and ARHGEF6 Complexes in Platelets. *J Biol Chem*.
811 290:29974-29983.
812 Nahidiazar, L., A.V. Agronskaia, J. Broertjes, B. van den Broek, and K. Jalink. 2016. Optimizing Imaging
813 Conditions for Demanding Multi-Color Super Resolution Localization Microscopy. *PLoS One*.
814 11:e0158884.
815 Nakahara, H., S.C. Mueller, M. Nomizu, Y. Yamada, Y. Yeh, and W.T. Chen. 1998. Activation of beta1
816 integrin signaling stimulates tyrosine phosphorylation of p190RhoGAP and membrane-
817 protrusive activities at invadopodia. *J Biol Chem*. 273:9-12.
818 Noll, B., D. Benz, Y. Frey, F. Meyer, M. Lauinger, S.A. Eisler, S. Schmid, P.L. Hordijk, and M.A. Olayioye.
819 2019. DLC3 suppresses MT1-MMP-dependent matrix degradation by controlling RhoB and actin
820 remodeling at endosomal membranes. *J Cell Sci*.
821 Oikawa, T., T. Itoh, and T. Takenawa. 2008. Sequential signals toward podosome formation in NIH-src
822 cells. *J Cell Biol*. 182:157-169.
823 Pan, S., Y. Deng, J. Fu, Y. Zhang, Z. Zhang, X. Ru, and X. Qin. 2018. Tumor Suppressive Role of ARHGAP17
824 in Colon Cancer Through Wnt/beta-Catenin Signaling. *Cell Physiol Biochem*. 46:2138-2148.
825 Pan, S.L., Y.Y. Deng, J. Fu, Y.H. Zhang, Z.J. Zhang, and X.J. Qin. 2022. ARHGAP17 enhances 5-Fluorouracil-
826 induced apoptosis in colon cancer cells by suppressing Rac1. *Neoplasma*.
827 Pichot, C.S., C. Arvanitis, S.M. Hartig, S.A. Jensen, J. Bechill, S. Marzouk, J. Yu, J.A. Frost, and S.J. Corey.
828 2010. Cdc42-interacting protein 4 promotes breast cancer cell invasion and formation of
829 invadopodia through activation of N-WASp. *Cancer Res*. 70:8347-8356.
830 Razidlo, G.L., B. Schroeder, J. Chen, D.D. Billadeau, and M.A. McNiven. 2014. Vav1 as a central regulator
831 of invadopodia assembly. *Curr Biol*. 24:86-93.
832 Reinhard, N.R., M. Mastop, T. Yin, Y. Wu, E.K. Bosma, T.W.J. Gadella, Jr., J. Goedhart, and P.L. Hordijk.
833 2017. The balance between Gα(i)-Cdc42/Rac and Gα(1)(2)/(1)(3)-RhoA pathways determines
834 endothelial barrier regulation by sphingosine-1-phosphate. *Mol Biol Cell*. 28:3371-3382.
835 Richnau, N., and P. Aspenstrom. 2001. Rich, a rho GTPase-activating protein domain-containing protein
836 involved in signaling by Cdc42 and Rac1. *J Biol Chem*. 276:35060-35070.
837 Richnau, N., A. Fransson, K. Farsad, and P. Aspenström. 2004. RICH-1 has a BIN/Amphiphysin/Rvsp
838 domain responsible for binding to membrane lipids and tubulation of liposomes. *Biochem*
839 *Biophys Res Commun*. 320:1034-1042.
840 Rossman, K.L., C.J. Der, and J. Sondek. 2005. GEF means go: turning on RHO GTPases with guanine
841 nucleotide-exchange factors. *Nat Rev Mol Cell Biol*. 6:167-180.
842 Sakurai-Yageta, M., C. Recchi, G. Le Dez, J.B. Sibarita, L. Daviet, J. Camonis, C. D'Souza-Schorey, and P.
843 Chavrier. 2008. The interaction of IQGAP1 with the exocyst complex is required for tumor cell
844 invasion downstream of Cdc42 and RhoA. *J Cell Biol*. 181:985-998.
845 Scott, R.W., D. Crighton, and M.F. Olson. 2011. Modeling and imaging 3-dimensional collective cell
846 invasion. *J Vis Exp*.
847 Stoletov, K., and J.D. Lewis. 2015. Invadopodia: a new therapeutic target to block cancer metastasis.
848 *Expert Rev Anticancer Ther*. 15:733-735.
849 Suman, P., S. Mishra, and H. Chander. 2018. High expression of FBP17 in invasive breast cancer cells
850 promotes invadopodia formation. *Med Oncol*. 35:71.
851 Takano, K., K. Toyooka, and S. Suetsugu. 2008. EFC/F-BAR proteins and the N-WASP-WIP complex induce
852 membrane curvature-dependent actin polymerization. *Embo j*. 27:2817-2828.
853 Tian, L., D.L. Nelson, and D.M. Stewart. 2000. Cdc42-interacting protein 4 mediates binding of the
854 Wiskott-Aldrich syndrome protein to microtubules. *J Biol Chem*. 275:7854-7861.

855 Tian, Q., H. Gao, Y. Zhou, L. Zhu, J. Yang, B. Wang, P. Liu, and J. Yang. 2022. RICH1 inhibits breast cancer
856 stem cell traits through activating kinases cascade of Hippo signaling by competing with Merlin
857 for binding to Amot-p80. *Cell Death & Disease*. 13:71.
858 Timmerman, I., N. Heemskerk, J. Kroon, A. Schaefer, J. van Rijssel, M. Hoogenboezem, J. van Unen, J.
859 Goedhart, T.W. Gadella, Jr., T. Yin, Y. Wu, S. Huveneers, and J.D. van Buul. 2015. A local VE-
860 cadherin and Trio-based signaling complex stabilizes endothelial junctions through Rac1. *J Cell*
861 *Sci*. 128:3041-3054.
862 Tonucci, F.M., E. Almada, C. Borini-Etichetti, A. Pariani, F. Hidalgo, M.J. Rico, J. Girardini, C. Favre, J.R.
863 Goldenring, M. Menacho-Marquez, and M.C. Larocca. 2019. Identification of a CIP4 PKA
864 phosphorylation site involved in the regulation of cancer cell invasiveness and metastasis.
865 *Cancer Lett*.
866 Tsujita, K., A. Kondo, S. Kurisu, J. Hasegawa, T. Itoh, and T. Takenawa. 2013. Antagonistic regulation of F-
867 BAR protein assemblies controls actin polymerization during podosome formation. *J Cell Sci*.
868 126:2267-2278.
869 Tsujita, K., S. Suetsugu, N. Sasaki, M. Furutani, T. Oikawa, and T. Takenawa. 2006. Coordination between
870 the actin cytoskeleton and membrane deformation by a novel membrane tubulation domain of
871 PCH proteins is involved in endocytosis. *J Cell Biol*. 172:269-279.
872 van Unen, J., T. Yin, Y.I. Wu, M. Mastop, T.W. Gadella, Jr., and J. Goedhart. 2016. Kinetics of recruitment
873 and allosteric activation of ARHGEF25 isoforms by the heterotrimeric G-protein Gαq. *Sci Rep*.
874 6:36825.
875 Vaughan, E.M., A.L. Miller, H.Y. Yu, and W.M. Bement. 2011. Control of local Rho GTPase crosstalk by
876 Abr. *Curr Biol*. 21:270-277.
877 Vinci, M., C. Box, and S.A. Eccles. 2015. Three-dimensional (3D) tumor spheroid invasion assay. *J Vis*
878 *Exp*:e52686.
879 Wells, C.D., J.P. Fawcett, A. Traweger, Y. Yamanaka, M. Goudreault, K. Elder, S. Kulkarni, G. Gish, C.
880 Virag, C. Lim, K. Colwill, A. Starostine, P. Metalnikov, and T. Pawson. 2006. A Rich1/Amot
881 complex regulates the Cdc42 GTPase and apical-polarity proteins in epithelial cells. *Cell*.
882 125:535-548.
883 Yamaguchi, H. 2012. Pathological roles of invadopodia in cancer invasion and metastasis. *Eur J Cell Biol*.
884 91:902-907.
885 Yamaguchi, H., M. Lorenz, S. Kempiak, C. Sarmiento, S. Coniglio, M. Symons, J. Segall, R. Eddy, H. Miki, T.
886 Takenawa, and J. Condeelis. 2005. Molecular mechanisms of invadopodium formation: the role
887 of the N-WASP-Arp2/3 complex pathway and cofilin. *J Cell Biol*. 168:441-452.
888 Yamamoto, H., M. Sutoh, S. Hatakeyama, Y. Hashimoto, T. Yoneyama, T. Koie, H. Saitoh, K. Yamaya, T.
889 Funyu, T. Nakamura, C. Ohyama, and S. Tsuboi. 2011. Requirement for FBP17 in invadopodia
890 formation by invasive bladder tumor cells. *J Urol*. 185:1930-1938.
891 Yu, X., T. Zech, L. McDonald, E.G. Gonzalez, A. Li, I. Macpherson, J.P. Schwarz, H. Spence, K. Futó, P.
892 Timpson, C. Nixon, Y. Ma, I.M. Anton, B. Visegrády, R.H. Insall, K. Oien, K. Blyth, J.C. Norman, and
893 L.M. Machesky. 2012. N-WASP coordinates the delivery and F-actin-mediated capture of MT1-
894 MMP at invasive pseudopods. *J Cell Biol*. 199:527-544.
895 Zagryazhskaya-Masson, A., P. Monteiro, A.S. Macé, A. Castagnino, R. Ferrari, E. Infante, A. Duperray-
896 Susini, F. Dingli, A. Lanyi, D. Loew, E. Génot, and P. Chavrier. 2020. Intersection of TKS5 and
897 FGD1/CDC42 signaling cascades directs the formation of invadopodia. *J Cell Biol*. 219.

898 Figure legends

899 **Figure 1. ARHGAP17 negatively regulates invadopodia.**

900 (**A**) Representative micrographs of a SUM159 cell with an invadopodia cluster. Cells were treated with
901 PDBu for 30 minutes and stained for cortactin and F-actin (scale bar for both panels, 5 µm). (**B**) shRNA
902 screen of candidate RhoGAPs in SUM159 cells. Cells stably expressing the indicated shRNAs were
903 treated with PDBu for 30 minutes and stained for cortactin and F-actin as invadopodia markers. Colors
904 represent different RhoGAPs, and individual bars represent unique shRNA targeting sequences. Results
905 are expressed as the percentage of cells with invadopodia from 4 images per condition for a total of
906 7100 cells. (**C**) Western blot of ARHGAP17 expression in SUM159 cells stably expressing non-targeting
907 and ARHGAP17-specific shRNAs. Tubulin was used as a loading control. (**D**) Percentage of cells with
908 invadopodia in CTRL or ARHGAP17 KD SUM159 cells treated with PDBu for 30 minutes. Results are
909 expressed as mean ± S.E.M. of 3 independent experiments in which at least 200 cells per condition per
910 experiment were counted. ***, $p<0.001$. (**E**) Western blot of ARHGAP17 KD and Rescue with shRNA-
911 resistant myc-ARHGAP17 in SUM159 cells. (**F**) Percentage of cells with invadopodia in CTRL, ARHGAP17
912 KD, and Rescue SUM159 cells treated PDBu for 30 minutes. Results are expressed as mean ± S.E.M. of 3
913 independent experiments in which at least 200 cells per condition per experiment were counted. **,
914 $p<0.01$; ns, not significant. (**G**) Representative micrographs of CTRL, ARHGAP17 KD, and Rescue with
915 myc-ARHGAP17 in SUM159 cells. F-actin and cortactin staining were used as markers for invadopodia
916 while myc staining was used to visualize myc-ARHGAP17. Cells were treated with PDBu for 30 minutes
917 before fixation and staining. Arrowheads highlight invadopodia clusters (scale bar, 20 µm).

918 **Figure 2. Loss of ARHGAP17 expression promotes invasion**

919 (**A**) Representative micrographs of SUM159 cells degrading a fluorescent-gelatin and collagen IV
920 substrate. F-actin staining was used as a marker for invadopodia. The zoomed panel on the right shows a
921 cluster of invadopodia colocalizing with degradation spots (scale bar for left and right panels, 10 µm). (**B**)
922 Representative micrographs of F-actin-stained SUM159 cells degrading fluorescent-gelatin and collagen
923 IV matrix after 24-hour PDBu treatment (scale bar, 20 µm). (**C**) Quantification of matrix degradation by
924 SUM159 cells. Results are expressed as mean ± S.E.M. of 3 independent experiments in which at least 20
925 random fields-of-view (FOV) per condition per experiment were measured. **, $p<0.01$; ns, not
926 significant. (**D**) Micrographs of SUM159 spheroids grown with Matrigel to promote invasion and without
927 Matrigel to observe spheroid growth (scale bar, 200 µm). (**E** and **F**) Quantification of spheroid size and
928 quantification of invasion corrected for proliferation. Results are expressed as mean ± S.E.M. of 4
929 independent experiments in which at least 5 spheroids per condition per experiment were measured. *,
930 $p<0.05$; ***, $p<0.001$; ns, not significant. (**G**) Z-view of inverse invasion assay of SUM159 cells expressing
931 Scarlet-CAAX with brightest point projection in the y-axis (scale bar, 20 µm). (**H**) Quantification of area
932 invaded by cells in the inverse invasion assay. Invasion was measured at 20 µm above the coverslip.
933 Results are expressed as mean ± S.E.M. of 3 independent experiments in which at least 3 FOV per
934 condition per experiment were measured. *, $p<0.05$; ***, $p<0.001$.

935 **Figure 3. ARHGAP17 knockdown increases invadopodia stability and accumulation.**

936 (**A**) Representative micrographs of SUM159 cells stained for F-actin (scale bar, 10 µm) and quantification
937 of percent invadopodia coverage after 30 min PDBu treatment. White dashed lines represent the cell
938 outline and yellow dashed lines represent invadopodia clusters. Results are expressed as mean ± S.E.M.
939 of 3 independent experiments in which at least 30 cells per condition per experiment were counted. *,
940 $p<0.05$; ns, not significant. (**B**) Time course of percentage of SUM159 cells forming invadopodia after
941 PDBu treatment at different intervals. Results are expressed as mean ± S.E.M. of 3 independent

942 experiments in which at least 200 cells per condition per experiment were counted. (**C**) Example of
943 single invadopodia dynamics showing assembly, stability, and disassembly phases as indicated by
944 measuring TKS5-mTagBFP2 intensity over time at 30 second intervals after PDBu treatment. The gray
945 line represents a second-order smoothing polynomial. (**D**) Representative micrographs of single
946 invadopodia dynamics of SUM159 cells expressing TKS5-mTagBFP2 as a marker for invadopodia after
947 PDBu treatment (scale bar, 1 µm). (**E-H**) Quantification of invadopodia dynamics. Results are expressed
948 as mean ± S.E.M. of 3 independent experiments in which at least 12 invadopodia per condition per
949 experiment were measured. Large circles represent biological replicates, small circles represent
950 technical replicates. *, $p<0.05$; **, $p<0.01$; ***, $p<0.001$; ns, not significant.

951 **Figure 4. ARHGAP17 localizes to invadopodia**

952 (**A**) Representative micrographs of CTRL and ARHGAP17 KO SUM159 cells stained for F-actin and
953 ARHGAP17. Arrowheads highlight invadopodia clusters (scale bar, 10 µm). (**B**) Representative TIRF
954 micrographs of a SUM159 cell expressing TKS5-mTagBFP2 as a marker for invadopodia and ARHGAP17-
955 GFP (expressed in ARHGAP17 KO cells) forming an invadopodia cluster after 30 min PDBu treatment
956 (scale bar for both panels, 5 µm). (**C**) STORM reconstructions of SUM159 cells treated with PDBu
957 showing myc-ARHGAP17 (expressed in ARHGAP17 KO cells) localization to invadopodia as defined by F-
958 actin staining (scale bar, 1 µm). (**D**) Quantification of STORM reconstructions using the radial intensity
959 analysis of F-actin, myc-ARHGAP17, cortactin, and paxillin in invadopodia. Lines are expressed as mean ±
960 S.E.M. of 3 independent experiments in which at least 20 invadopodia per condition per experiment
961 were measured.

962 **Figure 5. ARHGAP17 targets invadopodia through both the N-BAR and proline-rich domains**

963 (**A**) Domain structure of ARHGAP17 and the ARHGAP17 mutants used in this study. (**B**) Representative
964 TIRF micrographs of individual invadopodia in SUM159 cells expressing ARHGAP17-GFP domain deletion
965 mutants in ARHGAP17 KO cells. Cells were treated with PDBu for 30 min and stained for F-actin as a
966 marker for invadopodia (scale bar, 0.5 µm). (**C**) Radial intensity analysis of F-actin and ARHGAP17-GFP
967 mutants in invadopodia. Lines are expressed as mean ± S.E.M. of 4 independent experiments in which at
968 least 26 invadopodia per condition per experiment were measured. (**D** and **E**) Quantification of
969 ARHGAP17 distance from the center of invadopodia based on peak intensity and quantification of
970 normalized intensity of ARHGAP17 at invadopodia. Results are expressed as mean ± S.E.M. of 4
971 independent experiments in which at least 26 invadopodia per condition per experiment were
972 measured. Large circles represent biological replicates, small circles represent technical replicates. *,
973 $p<0.05$; ***, $p<0.001$. (**F**) Percentage of cells with invadopodia in CTRL, ARHGAP17 KO, and Rescue with
974 ARHGAP17 domain deletion mutants after 30 minutes PDBu treatment. Results are expressed as mean ±
975 S.E.M. of 3 independent experiments in which at least 200 cells per condition per experiment were
976 counted. Statistical analysis is a 1-way ANOVA with a Tukey's post hoc test. Different letters indicate
977 significant differences between conditions as defined by $p<0.05$.

978 **Figure 6. ARHGAP17 Cdc42-specific catalytic activity is required for its function at invadopodia**

979 (**A**) Pulldown of endogenous ARHGAP17 in SUM159 cells using constitutively active RhoA (Q63L), Rac1
980 (Q61L), and Cdc42 (Q61L) tagged with Glutathione S-transferase (GST) or with GST alone. (**B**) Pulldown
981 of active Cdc42 using the p21 binding domain (PBD) of p21 activated kinase 1 protein (PAK). Results are
982 expressed as mean ± S.E.M. of 4 independent experiments. ***, $p<0.001$; ns, not significant. (**C**) PBD

983 pulldown of active Cdc42 in SUM159 cells after treatment with PDBu at the indicated time points. Left
984 panel shows a representative WB; right panel shows the quantification of 3 independent experiments.
985 Results are expressed as mean ± S.E.M. *, p<0.05; ns, not significant. (**D**) Representative TIRF
986 micrographs of ARHGAP17 KO SUM159 cells forming single invadopodia after PDBu treatment stained
987 for F-actin as a marker for invadopodia and expressing either WT or catalytic dead (CD) ARHGAP17-GFP
988 (expressed in ARHGAP17 KO background) (scale bar, 0.5 µm). (**E**) Radial intensity analysis of F-actin, WT
989 ARHGAP17-GFP, and CD ARHGAP17-GFP in invadopodia. Lines are expressed as mean ± S.E.M. of 3
990 independent experiments in which at least 40 invadopodia per condition per experiment were
991 measured. (**F** and **G**) Quantification of ARHGAP17-GFP distance from the center of invadopodia based on
992 peak intensity and normalized intensity of ARHGAP17 at invadopodia. Results are expressed as mean ±
993 S.E.M. of 3 independent experiments in which at least 40 invadopodia per condition per experiment
994 were measured. Large circles represent biological replicates, small circles represent technical replicates.
995 ns, not significant. (**H**) Percentage of cells with invadopodia in CTRL, ARHGAP17 KO, and Rescue with
996 either WT or CD ARHGAP17-GFP after 30 minutes PDBu treatment. Results are expressed as mean ±
997 S.E.M. of 3 independent experiments in which at least 200 cells per condition per experiment were
998 counted. **, p<0.01; ns, not significant.

999 **Figure 7. ARHGAP17 regulates the spatiotemporal dynamics of Cdc42 activity during invadopodia**
1000 **turnover**

1001 (**A**) Representative TIRF micrographs of a SUM159 cell expressing TKS5-mTagBFP2 as a marker for
1002 invadopodia and dTomato-wGBD as a marker for Cdc42 activity and forming an invadopodia cluster
1003 after PDBu treatment (scale bar for both panels, 5 µm). (**B**) Representative TIRF micrographs of a
1004 SUM159 cell forming an individual invadopodia after PDBu treatment. Cells were expressing TKS5-
1005 mTagBFP2 as a marker for invadopodia, ARHGAP17-GFP (expressed in ARHGAP17 KO cells), and
1006 dTomato-wGBD as a marker for Cdc42 activity (scale bar, 1 µm). (**C**) Quantification of TKS5-mTagBFP2,
1007 ARHGAP17-GFP (expressed in ARHGAP17 KO cells), and dTomato-wGBD intensity at individual
1008 invadopodia. Intensity and time have been rescaled between values of 0 and 1 for each invadopodia to
1009 allow for comparison. Lines are loess smoothing and 95% confidence from 3 independent experiments
1010 in which at least 10 invadopodia per condition per experiment were measured. (**D**) Cross-correlation
1011 analysis of TKS5-mTagBFP2, ARHGAP17-GFP (expressed in ARHGAP17 KO background), and dTomato-
1012 wGBD intensity. Higher values denote positive correlation and lag denotes the time shift effect on
1013 correlation between signals. Lines are loess smoothing and 95% confidence from 3 independent
1014 experiments in which at least 10 invadopodia per condition per experiment were measured. (**E**)
1015 Quantification of the peak dTomato-wGBD intensity at individual invadopodia after PDBu treatment,
1016 normalized to the average whole-cell intensity before treatment. Results are expressed as mean ±
1017 S.E.M. of 3 independent experiments. Large circles represent biological replicates, small circles
1018 represent technical replicates. *, p<0.05; ns, not significant. (**F**) Radial intensity profiles of individual
1019 invadopodia from live cells expressing TKS5-mTagBFP2, ARHGAP17-GFP (expressed in ARHGAP17 KO
1020 cells), and dTomato-wGBD plotted over time. Time scales between invadopodia are rescaled between 0
1021 and 1 to allow for alignment of intensity values. Results are expressed as the mean of 8 representative
1022 invadopodia. (**G** and **H**) Radial profile plots taken from time 0.25 and 0.75 of panel (F) showing relative
1023 intensity and localization of the invadopodia markers while the invadopodia are assembling and
1024 disassembling, respectively. Results are expressed as mean ± S.E.M. of 8 invadopodia. (**I**) Radial intensity
1025 profiles of individual invadopodia from live cells expressing TKS5-mTagBFP2 and ΔC-ARHGAP17-GFP

1026 (expressed in ARHGAP17 KO cells) plotted over time. Time scales between invadopodia are rescaled
1027 between 0 and 1 to allow for alignment of intensity values. Results are expressed as the mean of 13
1028 representative invadopodia. (**J** and **K**) Radial profile plots taken from time 0.25 and 0.75 of panel (I)
1029 showing relative intensity and localization of the invadopodia markers while the invadopodia are
1030 assembling and disassembling, respectively. Results are expressed as mean ± S.E.M. of 13 invadopodia.

1031 **Figure 8. ARHGAP17 interacts with CIP4 to regulate invadopodia**

1032 (**A**) Representative western blot of CIP4 expression in SUM159 cells expressing non-targeting (CTRL) or
1033 CIP4-specific shRNAs. (**B**) Representative micrographs of CTRL and CIP4 KD (shRNA #4) SUM159 cells. F-
1034 actin and cortactin staining were used as markers for invadopodia. Cells were treated with PDBu for 30
1035 minutes before fixation and staining. Arrowheads highlight invadopodia clusters (scale bar, 20 µm). (**C**)
1036 Percentage of cells with invadopodia in CTRL and CIP4 KD SUM159 cells treated PDBu for 30 minutes.
1037 Results are expressed as mean ± S.E.M. of 3 independent experiments in which at least 200 cells per
1038 condition per experiment were counted. *, $p<0.05$; **, $p<0.01$. (**D**) Representative micrographs of
1039 SUM159 cells treated with PDBu for 30 min and stained for F-actin and endogenous CIP4 (scale bar, 10
1040 µm). (**E**) Radial intensity analysis of F-actin and CIP4 in invadopodia. Lines are expressed as mean ±
1041 S.E.M. of 3 independent experiments in which at least 10 invadopodia per condition per experiment
1042 were measured. (**F**) Western blot of co-immunoprecipitation of endogenous ARHGAP17 and CIP4 in
1043 SUM159 cells. (**G**) Western blot of co-immunoprecipitation of myc-CIP4 with GFP, ΔC ARHGAP17-GFP, or
1044 WT ARHGAP17-GFP. (**H**) Western blot of affinity precipitation of myc-CIP4 and CD ARHGAP17-GFP using
1045 GST-Cdc42-Q61L bound to Glutathione Sepharose 4B.

1046 **Figure 9. Spatiotemporal dynamics of CIP4 and ARHGAP17**

1047 (**A**) Representative TIRF micrographs of a SUM159 cell forming a single invadopodia after PDBu
1048 treatment expressing TKS5-mTagBFP2 as a marker for invadopodia, CIP4-GFP (expressed in CIP4 KD
1049 cells), and dTomato-wGBD as a marker for Cdc42 activity (scale bar, 0.5 µm). (**B**) Quantification of TKS5-
1050 mTagBFP2, CIP4-GFP (expressed in CIP4 KD cells), and dTomato-wGBD intensity at individual
1051 invadopodia. Intensity and time were rescaled between values of 0 and 1 for each invadopodia to allow
1052 for comparison. Lines are loess smoothing and 95% confidence from 3 independent experiments in
1053 which at least 10 invadopodia per condition per experiment were measured. (**C**) Cross-correlation
1054 analysis of TKS5-mTagBFP2, CIP4-GFP (expressed in CIP4 KD cells), and dTomato-wGBD intensity. Higher
1055 values denote positive correlation and lag denotes the time shift effect on correlation between signals.
1056 Lines are loess smoothing and 95% confidence from 3 independent experiments in which at least 10
1057 invadopodia per condition per experiment were measured. (**D**) Representative TIRF micrographs of
1058 ARHGAP17 KO SUM159 cells transfected with the indicated constructs and treated with PDBu for 30
1059 min. Cells were fixed and stained for F-actin and myc to detect myc-CIP4 (scale bar, 10 µm). (**E**) Radial
1060 intensity analysis of F-actin, ARHGAP17-GFP, and myc-CIP4 in invadopodia. Lines are expressed as mean
1061 ± S.E.M. of 3 independent experiments in which at least 10 invadopodia per condition per experiment
1062 were measured. (**F**) Van Steensil's cross-correlation function of ARHGAP17-GFP colocalization with myc-
1063 CIP4 or the background signal of the anti-myc antibody at invadopodia clusters in SUM159 cells treated
1064 with PDBu for 30 min. Shift denotes the x-dimension movement of one channel in relation to the other.
1065 Lines are loess smoothing and 95% confidence from 3 independent experiments in which at least 10
1066 invadopodia clusters per condition per experiment were measured. (**G**) Invadopodia assay of SUM159
1067 cells after 30 minutes PDBu treatment in which CIP4 and ARHGAP17 were either silenced and/or

1068 overexpressed in all possible combinations as indicated in the graph. Results are expressed as mean ±
1069 S.E.M. of 3 independent experiments in which at least 200 cells per condition per experiment were
1070 counted. Statistical analysis is a 1-way ANOVA with a Tukey's post hoc test. Different letters indicate
1071 significant differences between conditions as defined by $p<0.05$.

1072 **Figure 10. Model of ARHGAP17 function in invadopodia**

1073 During invadopodia assembly/maturation, ARHGAP17 is present at the invadopodia ring, which helps to
1074 restrict Cdc42 activity to the invadopodia core. Cdc42 is activated by a specific GEF at the invadopodia
1075 core, most likely FGD1, where it promotes actin nucleation through binding to N-WASP and CIP4 and
1076 stimulates degradation through its interaction with IQGAP. ARHGAP17 moves to the invadopodia core
1077 by binding to CIP4 where it inactivates Cdc42 to promote invadopodia disassembly.

1078 Video figure legends

1079 **Video 1. SUM159 cell forming invadopodia after PDBu treatment**

1080 Live TIRF imaging of a SUM159 cell expressing TKS5-mTagBFP2 and treated with PDBu (scale bar, 10
1081 µm).

1082 **Video 2. SUM159 cell inverse invasion assay**

1083 Live spinning-disk z-projection of SUM159 cells expressing mScarlet-CAAX invading into Matrigel (scale
1084 bar, 10 µm).

1085 **Video 3. ARHGAP17 localizes to invadopodia**

1086 Live TIRF imaging of a SUM159 cell expressing TKS5-mTagBFP2 and ARHGAP17-GFP (expressed in
1087 ARHGAP17 KO background), treated with PDBu (scale bar, 10 µm).

1088 **Video 4. dTomato-wGBD sensor localization to membrane protrusions**

1089 Live TIRF imaging of membrane protrusions from SUM159 cells expressing either dTomato as a control
1090 for cytoplasmic localization or dTomato-wGBD (scale bar, 5 µm).

1091 **Video 5. dTomato-wGBD sensor localizes to invadopodia.**

1092 Live TIRF imaging of a SUM159 cell expressing TKS5-mTagBFP2 and dTomato-wGBD, treated with PDBu
1093 (scale bar, 10 µm).

1094 **Video 6. dTomato does not localize to invadopodia.**

1095 Live TIRF imaging of a SUM159 cell expressing TKS5-mTagBFP2 and dTomato, treated with PDBu (scale
1096 bar, 10 µm).

1097 **Video 7. Localization of ARHGAP17 and Cdc42 activity at an individual invadopodia.**

1098 Live TIRF of an individual invadopodia from a SUM159 cells expressing TKS5-mTagBFP2, ARHGAP17-GFP
1099 (expressed in ARHGAP17 KO background), and dTomato-wGBD, treated with PDBu (scale bar, 1 µm).

1100 **Video 8. Localization of CIP4 and Cdc42 activity at an individual invadopodia.**

1101 Live TIRF of an individual invadopodia from a SUM159 cells expressing TKS5-mTagBFP2, GFP-CIP4, and
1102 dTomato-wGBD, treated with PDBu (scale bar, 1 µm).

1103 Supplementary figure legends

1104 **Figure S1. ARHGAP17 KO validation**

1105 (**A**) Representative western blot showing loss of ARHGAP17 protein in SUM159 cells using two different
1106 gRNA targets. (**B**) Percentage of cells with invadopodia after treatment with PDBu for 30 minutes.
1107 Results are expressed as mean ± S.E.M. of 3 independent experiments in which at least 200 cells per
1108 condition per experiment were counted. **, p<0.01.

1109 **Figure S2. ARHGAP17 KD increases the formation of spontaneous invadopodia**

1110 (**A**) Representative micrographs of ARHGAP17 knockdown and Rescue with shRNA resistant myc-
1111 ARHGAP17 in SUM159 cells. F-actin and cortactin staining were used as markers for invadopodia while
1112 myc staining was used to visualize myc-ARHGAP17. Arrowheads highlight invadopodia clusters (scale
1113 bar, 20 µm). (**B**) Percentage of cells with invadopodia after treatment with PDBu for 30 minutes. Results
1114 are expressed as mean ± S.E.M. of 3 independent experiments in which at least 200 cells per condition
1115 per experiment were counted. **, p<0.01; ns, not significant.

1116 **Figure S3. ARHGAP17 KD reduces invadopodia turnover**

1117 (**A**) Quantification of change in percentage of cells forming invadopodia between peak invadopodia
1118 formation 10 minutes after PDBu treatment and equilibrium at 30 minutes after PDBu treatment.
1119 Results are expressed as mean ± S.E.M. of 3 independent experiments in which at least 200 cells per
1120 condition per experiment were counted. *, p<0.05; **, p<0.01; ns, not significant.

1121 **Figure S4. ARHGAP17 regulates invadopodia lifetime and stability**

1122 (**A**) Quantification of invadopodia lifetime in untreated SUM159 cells. Results are expressed as mean ±
1123 S.E.M of at least 40 invadopodia per condition. ***, p<0.001. (**B** and **C**) Quantification of invadopodia
1124 assembly and disassembly rate. Results are expressed as mean ± S.E.M. of 3 independent experiments.
1125 Large circles represent biological replicates, small circles represent technical replicates. ns, not
1126 significant. (**D**) Principal component analysis of invadopodia dynamics. The ellipses represent 95%
1127 confidence.

1128 **Figure S5. Paxillin and cortactin localization to invadopodia**

1129 (**A** and **B**) STORM reconstructions of SUM159 cells treated with PDBu showing cortactin and paxillin
1130 localization to invadopodia as defined by F-actin staining (scale bar, 1 µm).

1131 **Figure S6. ARHGAP17-GFP localization at invadopodia in untreated cells**

1132 (**A**) Example micrograph of a SUM159 cell invadopodia cluster expressing TKS5-mTagBFP2 and
1133 ARHGAP17-GFP in an ARHGAP17 KO background (scale bar, 1 µm). (**B**) Radial intensity analysis of TKS5-
1134 mTagBFP2 and ARHGAP17-GFP at invadopodia. Lines are expressed as mean ± S.E.M. of 3 independent
1135 experiments in which at least 10 invadopodia per condition per experiment were measured.

1136 **Figure S7. Localization of ARHGAP17 domain deletion mutants**

1137 (**A**) Representative TIRF micrographs of SUM159 cells expressing ARHGAP17-GFP domain deletion
1138 mutants in an ARHGAP17 KO background. Cells were treated with PDBu for 30 min and stained for F-
1139 actin as a marker for invadopodia. Arrowheads highlight invadopodia clusters (scale bar for both panels,
1140 10 µm).

1141 **Figure S8. Cdc42 activity in ARHGAP17 KD cells**

1142 (**A**) PBD pulldown of active Cdc42 in ARHGAP17 KD SUM159 cells after treatment with PDBu at the
1143 indicated time points. Results are expressed as mean ± S.E.M. of 3 independent experiments. *, $p<0.05$;
1144 ns, not significant.

1145 **Figure S9. Localization of ARHGAP17 CD**

1146 (**A**) Representative TIRF micrographs of SUM159 cells expressing FL-ARHGAP17-GFP and CD-ARHGAP17-
1147 GFP in an ARHGAP17 KO background. Cells were treated with PDBu for 30 min and stained for F-actin as
1148 a marker for invadopodia. Arrowheads highlight invadopodia clusters (scale bar for both panels, 10 µm).

1149 **Figure S10. Cdc42 FRET biosensor activity at invadopodia**

1150 (**A**) Representative micrographs of a SUM159 cell expressing the single-chain Cdc42 FRET biosensor and
1151 mCherry-cortactin as a marker for invadopodia after PDB treatment (scale bar, 5 µm). The color
1152 calibration bar indicates the relative FRET ratio. White arrowheads indicate invadopodia cluster, yellow
1153 arrowheads indicate lamellipodia protrusion. (**B**) Quantification of FRET ratio and mCherry-cortactin
1154 intensity at individual invadopodia. Intensity and time have been rescaled between values of 0 and 1 for
1155 each invadopodia to allow for comparison. Lines are loess smoothing and 95% confidence from 5
1156 invadopodia. (**C**) Example frame highlighting Cdc42 FRET at invadopodia in a SUM159 cell as marked by
1157 mCherry-cortactin (scale bar, 5 µm). (**D**) Radial intensity analysis of FRET ratio and mCherry-cortactin
1158 intensity at invadopodia. Lines are expressed as mean ± S.E.M. of 40 invadopodia.

1159 **Figure S11. Validation of the Cdc42 biosensor specificity**

1160 (**A**) Design of the Cdc42 activity biosensor used in this study, composed of the GTPase-binding domain of
1161 WASP (wGBD) tagged with dTomato. (**B**) Representative micrographs of SUM159 cells showing
1162 colocalization of the dTomato-wGBD sensor with different mTurquoise2-H2A-RhoGTPase-ΔCAAX
1163 constructs (RhoA-G14V, Rac1-G12V, or Cdc42-G12V) (scale bar, 10 µm). (**C**) Quantification of the average
1164 intensity of dTomato-wGBD signal within the nucleus ratioed to the average intensity in the cytosol.
1165 Results are mean ± S.D. of at least 14 cells per condition from 3 independent experiments. ****,
1166 $p<0.0001$; ns, not significant. (**D**) Representative TIRF micrographs of lamellipodia protrusions from
1167 SUM159 cells expressing either dTomato as a control for cytoplasmic localization or dTomato-wGBD
1168 (scale bar, 5 µm). (**E**) Quantification of panel (D) in which a 10-pixel wide line was drawn perpendicular
1169 to the cell edge (yellow dashed line in panel D) and the intensity was measured for each frame. Distance
1170 0 starts 10-15 µm within the cell and the protrusion can be visualized by a change in distance at intensity
1171 0.25 over time. The increase in peak dTomato-wGBD intensity over time indicates an increase in Cdc42
1172 activity localized to the leading edge.

1173 **Figure S12. Control for dTomato-wGBD invadopodia localization**

1174 (**A**) Representative TIRF micrographs of a SUM159 cell expressing TKS5-mTagBFP2 as a marker for
1175 invadopodia and dTomato as a localization control for the dTomato-wGBD biosensor forming an
1176 invadopodia cluster after PDBu treatment (scale bar for both panels, 5 µm).

Fig. 1

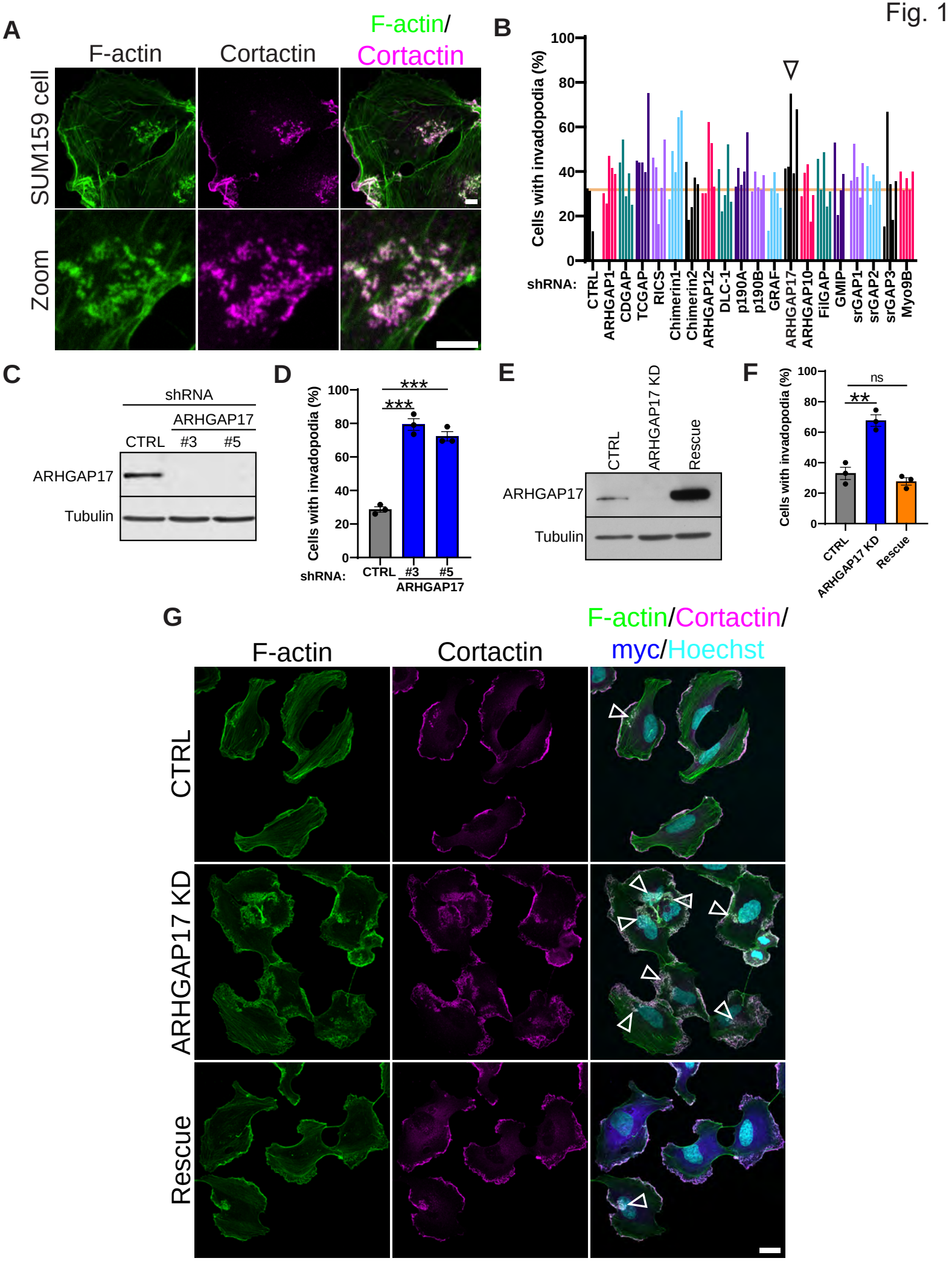
A
F-actin
Cortactin
F-actin/
Cortactin
SUM159 cell
Zoom
B
Cells with invadopodia (%)
shRNA:
CTRL
ARHGAP1
CDGAP
TCGAP
RICS
Chimerin1
Chimerin2
ARHGAP12
DLC-1
p190A
p190B
GRAF
ARHGAP17
ARHGAP10
FilGAP
GMIP
srGAP1
srGAP2
srGAP3
Myo9B
C
shRNA
ARHGAP17
CTRL
#3
#5
ARHGAP17
Tubulin
D
Cells with invadopodia (%)
***
***
shRNA:
CTRL
#3
#5
ARHGAP17
E
CTRL
ARHGAP17 KD
Rescue
ARHGAP17
Tubulin
F
Cells with invadopodia (%)
ns
**
CTRL
ARHGAP17 KD
Rescue
G
F-actin
Cortactin
F-actin/Cortactin/
myc/Hoechst
CTRL
ARHGAP17 KD
Rescue

Fig. 2

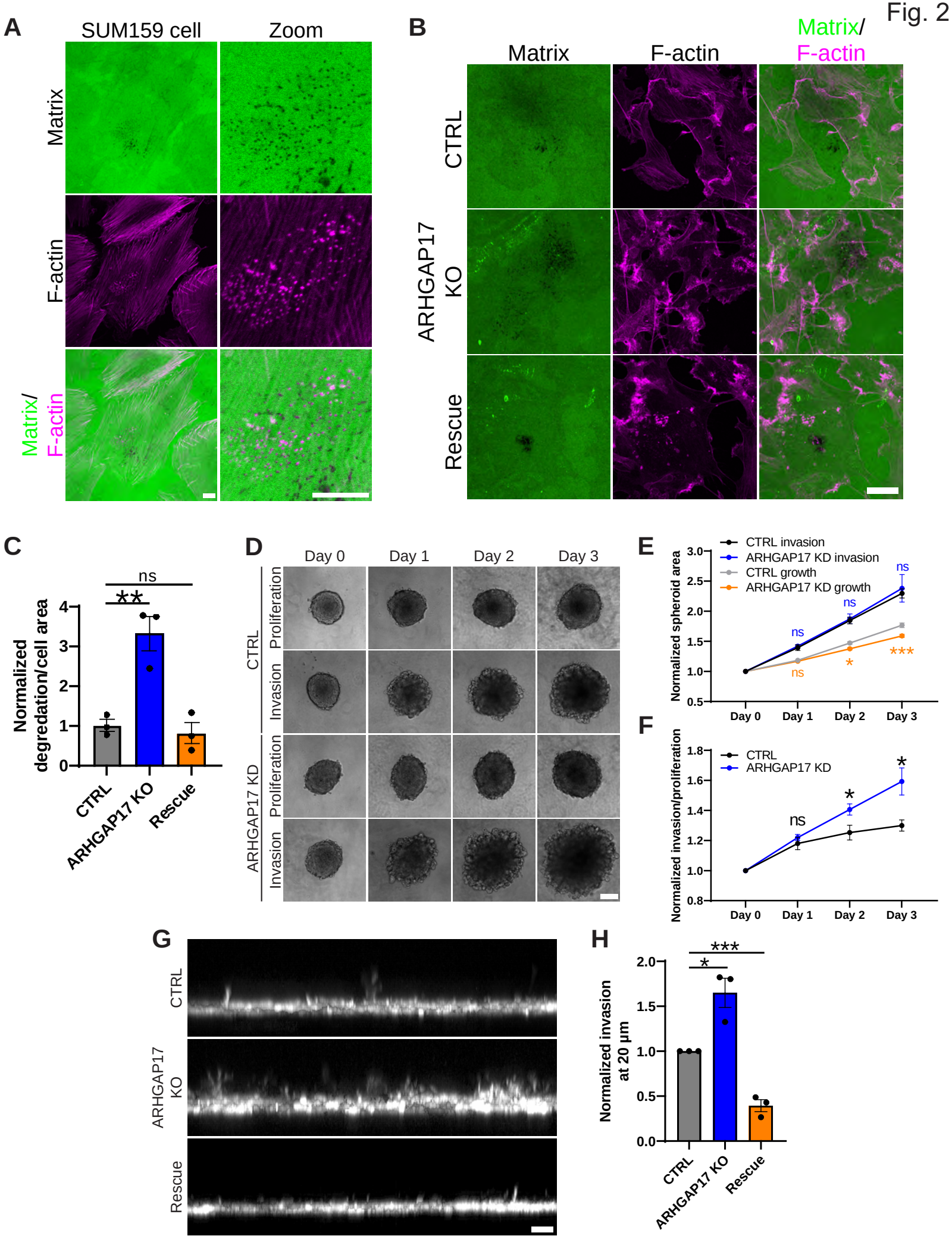
A
SUM159 cell
Zoom
Matrix
F-actin
Matrix/
F-actin
B
Matrix
F-actin
Matrix/
F-actin
CTRL
ARHGAP17
KO
Rescue
C
ns
**
Normalized
degredation/cell area
CTRL
ARHGAP17 KO
Rescue
D
Day 0
Day 1
Day 2
Day 3
CTRL
Proliferation
Invasion
ARHGAP17 KD
Proliferation
Invasion
E
CTRL invasion
ARHGAP17 KD invasion
CTRL growth
ARHGAP17 KD growth
Normalized spheroid area
ns
ns
ns
ns
*
***
Day 0
Day 1
Day 2
Day 3
F
CTRL
ARHGAP17 KD
Normalized invasion/proliferation
ns
*
*
Day 0
Day 1
Day 2
Day 3
G
CTRL
ARHGAP17
KO
Rescue
H
***
*
Normalized invasion
at 20 µm
CTRL
ARHGAP17 KO
Rescue

Fig. 3

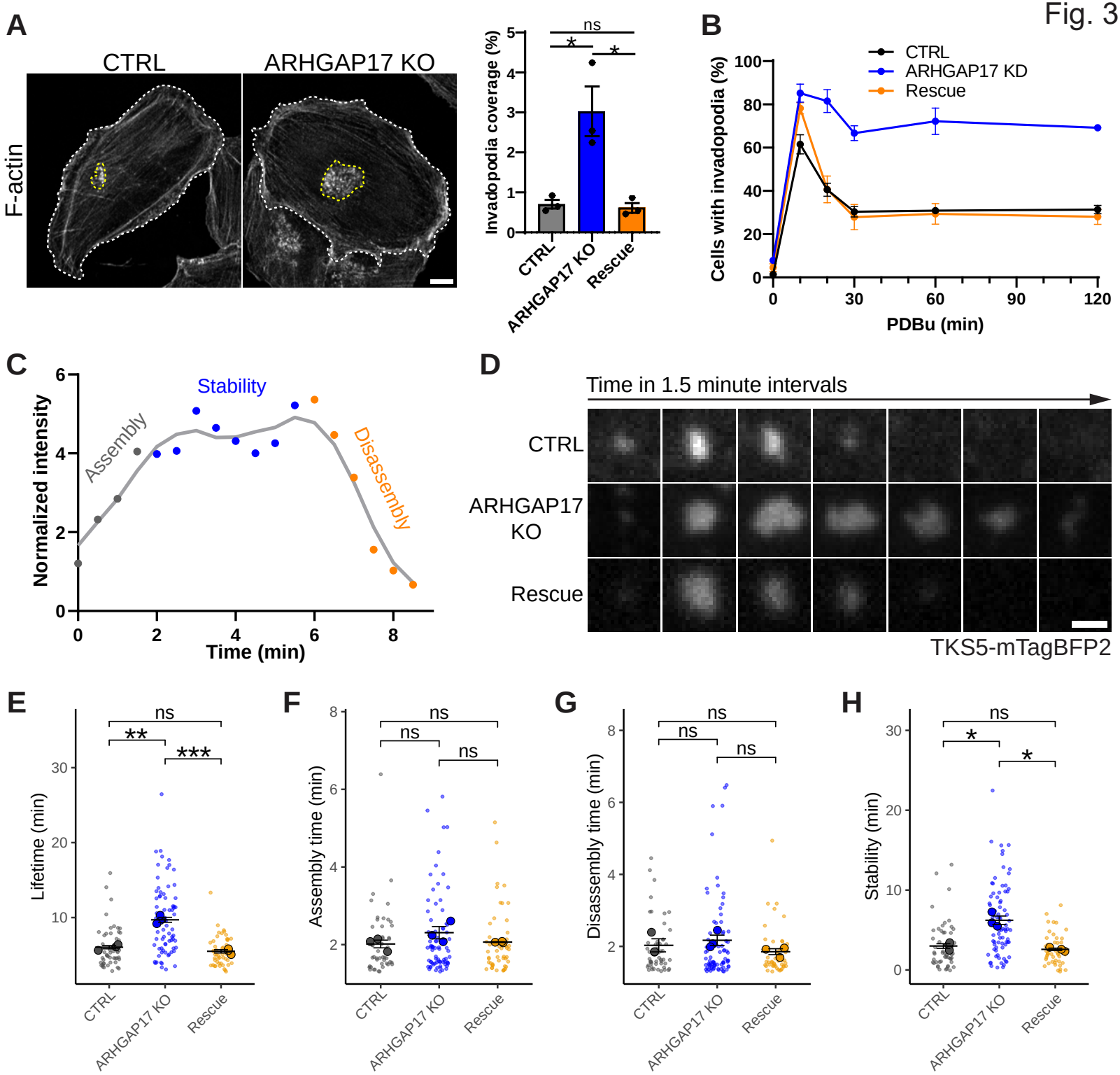
A
CTRL
ARHGAP17 KO
F-actin
Invadopodia coverage (%)
ns
*
*
CTRL
ARHGAP17 KO
Rescue
B
CTRL
ARHGAP17 KD
Rescue
Cells with invadopodia (%)
PDBu (min)
C
Stability
Assembly
Disassembly
Normalized intensity
Time (min)
D
Time in 1.5 minute intervals
CTRL
ARHGAP17 KO
Rescue
TKS5-mTagBFP2
E
Lifetime (min)
ns
**
***
F
Assembly time (min)
ns
ns
ns
G
Disassembly time (min)
ns
ns
ns
H
Stability (min)
ns
*
*
CTRL
ARHGAP17 KO
Rescue

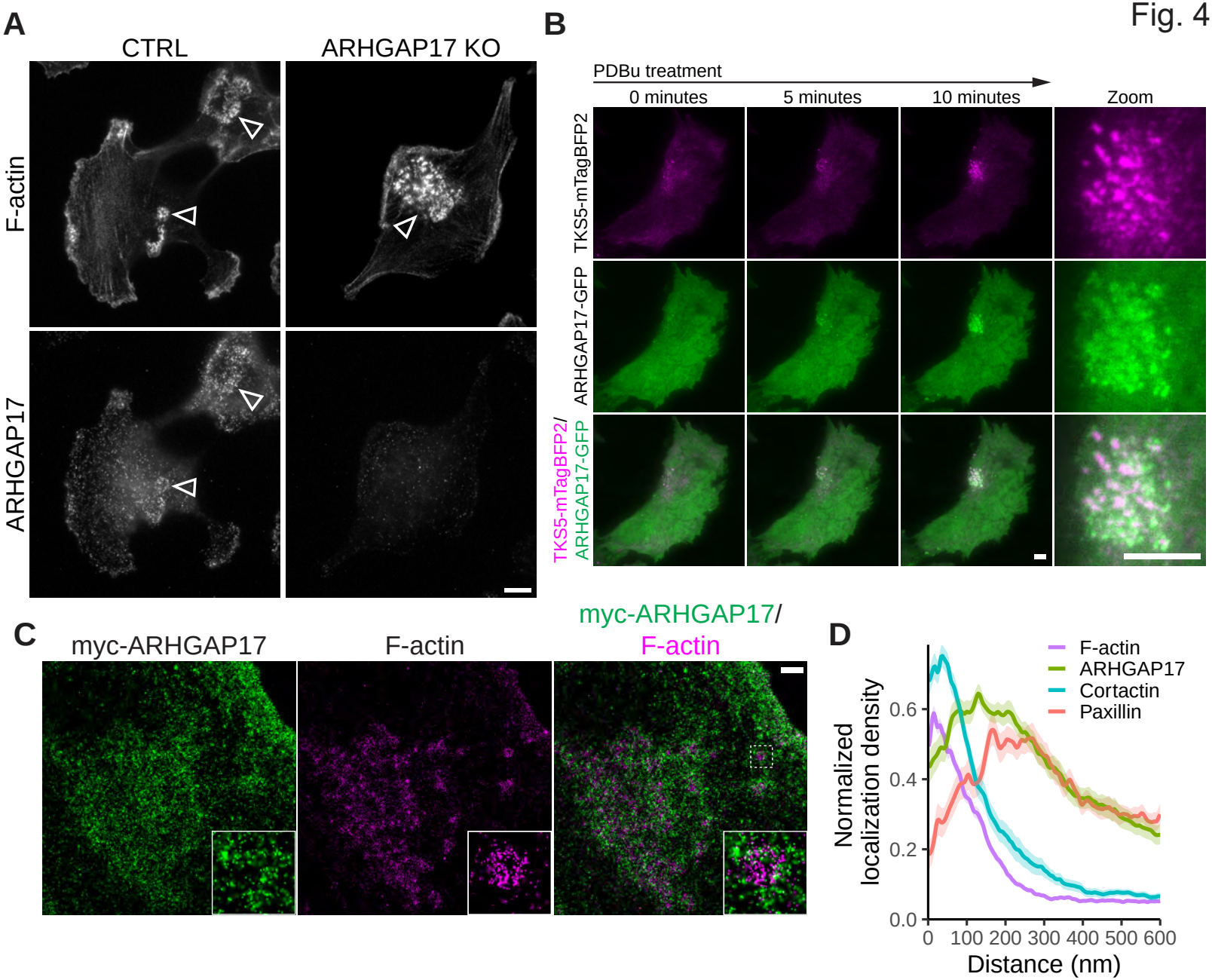
A
CTRL
ARHGAP17 KO
F-actin
ARHGAP17
B
PDBu treatment
0 minutes
5 minutes
10 minutes
Zoom
TKS5-mTagBFP2
ARHGAP17-GFP
TKS5-mTagBFP2/
ARHGAP17-GFP
C
myc-ARHGAP17
F-actin
myc-ARHGAP17/
F-actin
D
F-actin
ARHGAP17
Cortactin
Paxillin
Normalized
localization density
0.0
0.2
0.4
0.6
0
100
200
300
400
500
600
Distance (nm)

Fig. 5

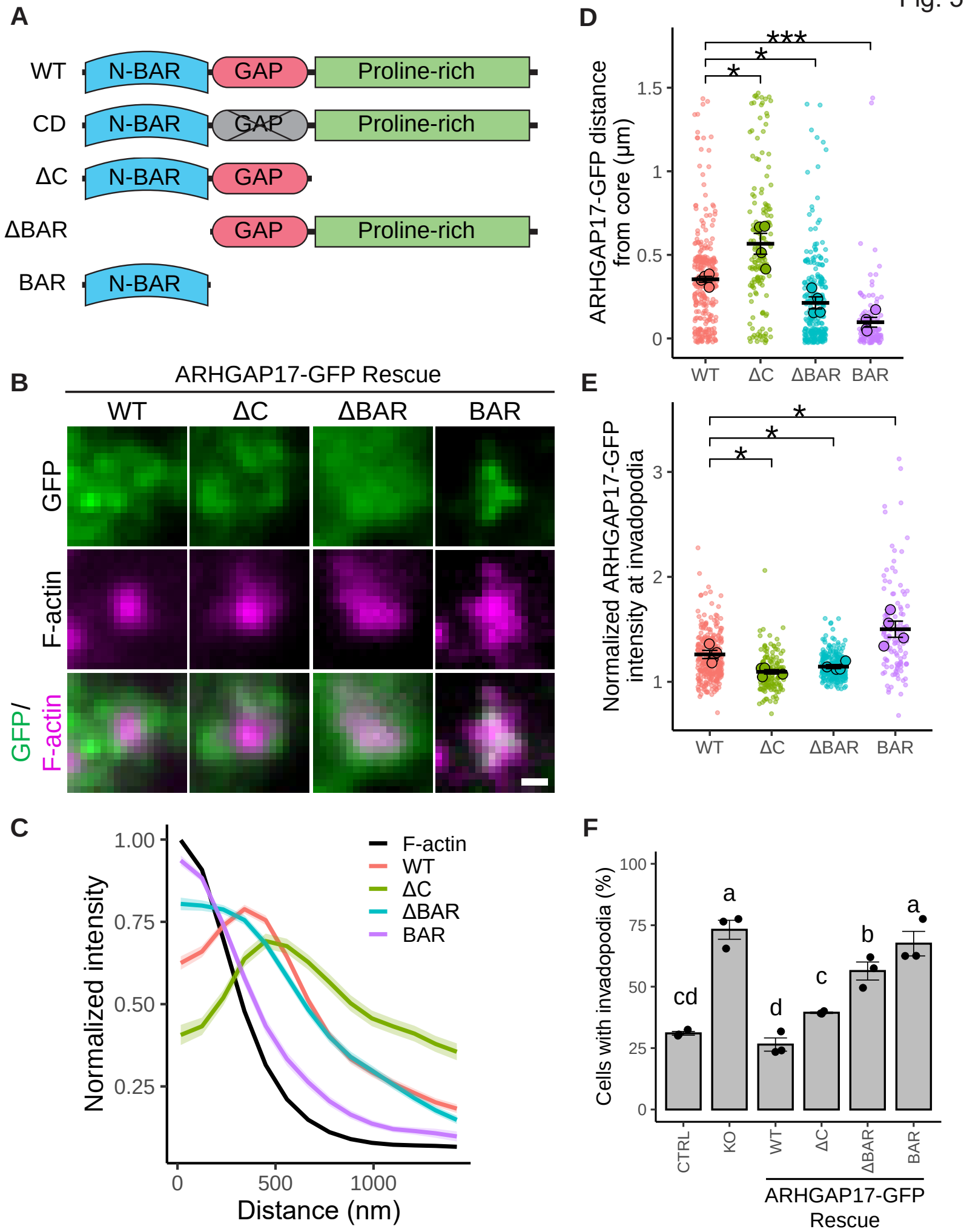
A
WT
N-BAR
GAP
Proline-rich
CD
N-BAR
GAP
Proline-rich
ΔC
N-BAR
GAP
ΔBAR
GAP
Proline-rich
BAR
N-BAR
B
ARHGAP17-GFP Rescue
WT
ΔC
ΔBAR
BAR
GFP
F-actin
GFP/
F-actin
C
Normalized intensity
1.00
0.75
0.50
0.25
0
500
1000
Distance (nm)
F-actin
WT
ΔC
ΔBAR
BAR
D
ARHGAP17-GFP distance from core (µm)
1.5
1
0.5
0
***
*
*
WT
ΔC
ΔBAR
BAR
E
Normalized ARHGAP17-GFP intensity at invadopodia
3
2
1
*
*
*
WT
ΔC
ΔBAR
BAR
F
Cells with invadopodia (%)
100
75
50
25
0
cd
a
d
c
b
a
CTRL
KO
WT
ΔC
ΔBAR
BAR
ARHGAP17-GFP Rescue

Fig. 6

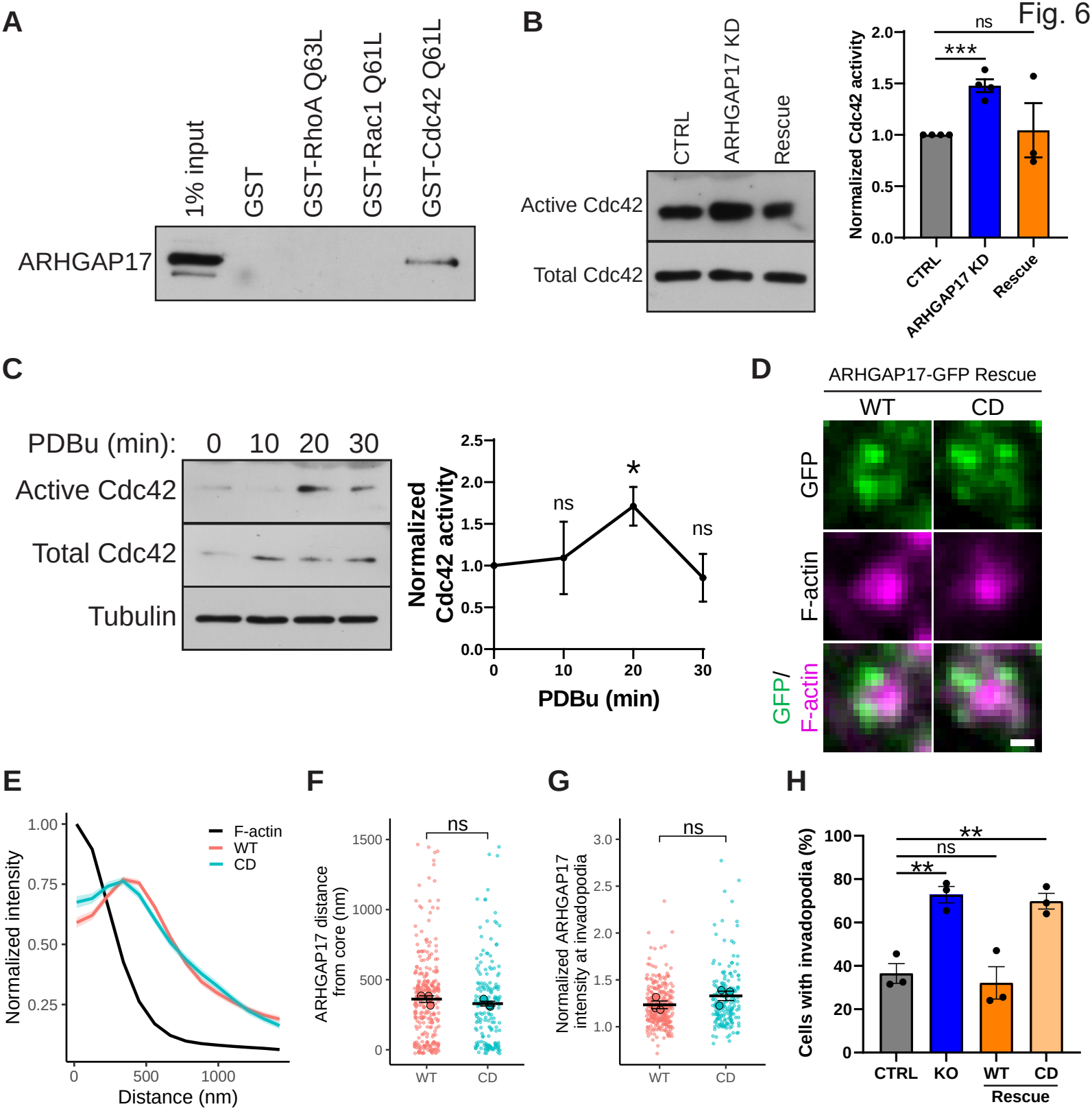
A
1% input
GST
GST-RhoA Q63L
GST-Rac1 Q61L
GST-Cdc42 Q61L
ARHGAP17
B
CTRL
ARHGAP17 KD
Rescue
Active Cdc42
Total Cdc42
Normalized Cdc42 activity
ns
***
CTRL
ARHGAP17 KD
Rescue
C
PDBu (min): 0 10 20 30
Active Cdc42
Total Cdc42
Tubulin
Normalized Cdc42 activity
ns
*
ns
PDBu (min)
D
ARHGAP17-GFP Rescue
WT
CD
GFP
F-actin
GFP/ F-actin
E
F-actin
WT
CD
Normalized intensity
Distance (nm)
F
ARHGAP17 distance from core (nm)
ns
WT
CD
G
Normalized ARHGAP17 intensity at invadopodia
ns
WT
CD
H
Cells with invadopodia (%)
**
ns
**
CTRL
KO
WT
CD
Rescue

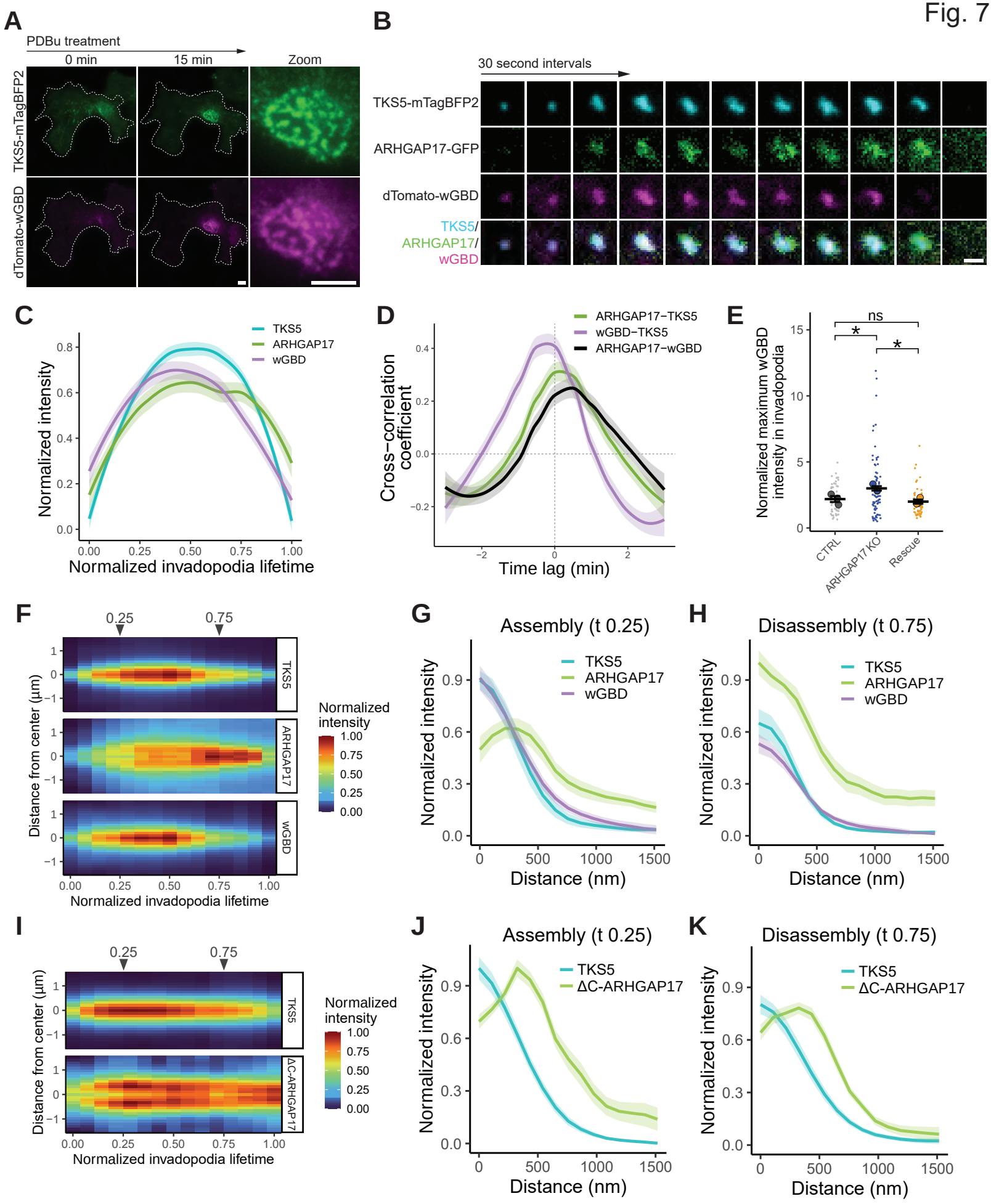
A
PDBu treatment
0 min
15 min
Zoom
TKS5-mTagBFP2
dTomato-wGBD
B
30 second intervals
TKS5-mTagBFP2
ARHGAP17-GFP
dTomato-wGBD
TKS5/
ARHGAP17/
wGBD
C
TKS5
ARHGAP17
wGBD
Normalized intensity
Normalized invadopodia lifetime
D
ARHGAP17−TKS5
wGBD−TKS5
ARHGAP17−wGBD
Cross−correlation coefficient
Time lag (min)
E
ns
*
*
Normalized maximum wGBD intensity in invadopodia
CTRL
ARHGAP17 KO
Rescue
F
0.25
0.75
TKS5
ARHGAP17
wGBD
Distance from center (µm)
Normalized intensity
Normalized invadopodia lifetime
G
Assembly (t 0.25)
TKS5
ARHGAP17
wGBD
Normalized intensity
Distance (nm)
H
Disassembly (t 0.75)
TKS5
ARHGAP17
wGBD
Normalized intensity
Distance (nm)
I
0.25
0.75
TKS5
ΔC-ARHGAP17
Distance from center (µm)
Normalized intensity
Normalized invadopodia lifetime
J
Assembly (t 0.25)
TKS5
ΔC-ARHGAP17
Normalized intensity
Distance (nm)
K
Disassembly (t 0.75)
TKS5
ΔC-ARHGAP17
Normalized intensity
Distance (nm)

Fig. 8

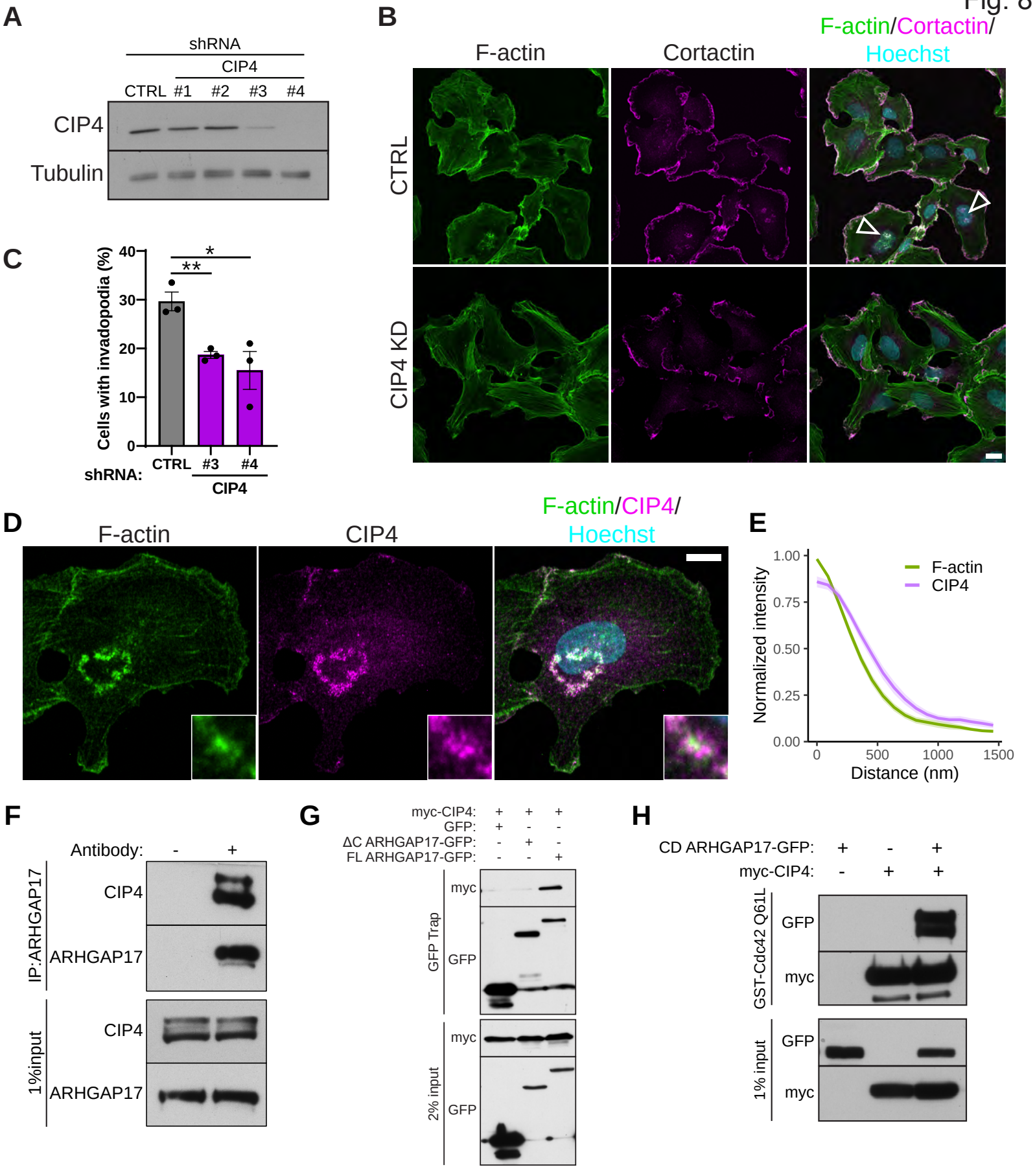
A
shRNA
CIP4
CTRL #1 #2 #3 #4
CIP4
Tubulin
B
F-actin
Cortactin
F-actin/Cortactin/
Hoechst
CTRL
CIP4 KD
C
Cells with invadopodia (%)
40
30
20
10
0
*
**
CTRL #3 #4
shRNA:
CIP4
D
F-actin
CIP4
F-actin/CIP4/
Hoechst
E
Normalized intensity
1.00
0.75
0.50
0.25
0.00
F-actin
CIP4
0 500 1000 1500
Distance (nm)
F
Antibody: - +
IP:ARHGAP17
CIP4
ARHGAP17
1%input
CIP4
ARHGAP17
G
myc-CIP4: + + +
GFP: + - -
ΔC ARHGAP17-GFP: - + -
FL ARHGAP17-GFP: - - +
GFP Trap
myc
GFP
2% input
myc
GFP
H
CD ARHGAP17-GFP: + - +
myc-CIP4: - + +
GST-Cdc42 Q61L
GFP
myc
1% input
GFP
myc

Fig. 9

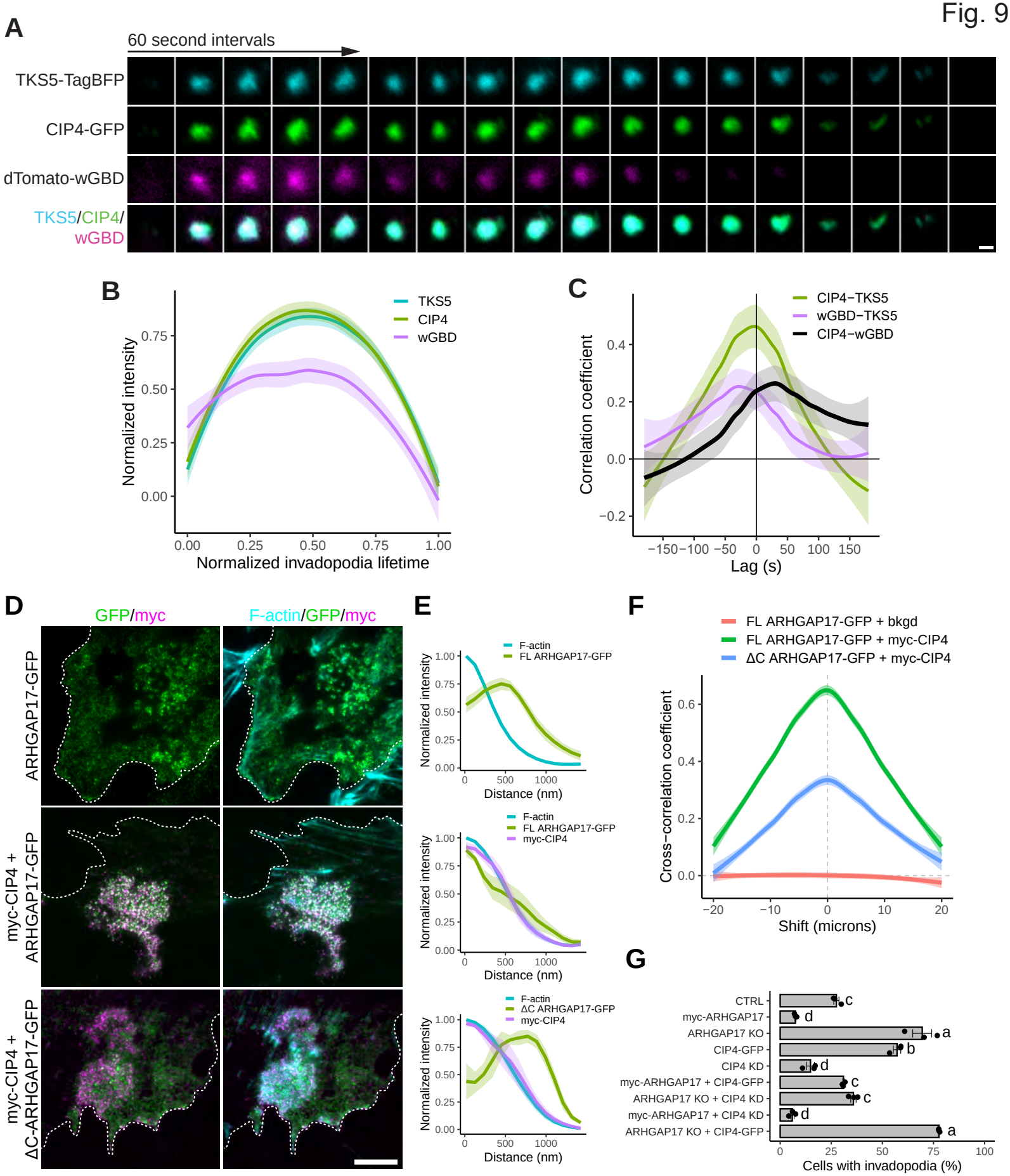
A
60 second intervals
TKS5-TagBFP
CIP4-GFP
dTomato-wGBD
TKS5/CIP4/
wGBD
B
TKS5
CIP4
wGBD
Normalized intensity
Normalized invadopodia lifetime
C
CIP4−TKS5
wGBD−TKS5
CIP4−wGBD
Correlation coefficient
Lag (s)
D
GFP/myc
F-actin/GFP/myc
ARHGAP17-GFP
myc-CIP4 +
ARHGAP17-GFP
myc-CIP4 +
ΔC-ARHGAP17-GFP
E
F-actin
FL ARHGAP17-GFP
myc-CIP4
ΔC ARHGAP17-GFP
Normalized intensity
Distance (nm)
F
FL ARHGAP17-GFP + bkgd
FL ARHGAP17-GFP + myc-CIP4
ΔC ARHGAP17-GFP + myc-CIP4
Cross−correlation coefficient
Shift (microns)
G
CTRL
myc-ARHGAP17
ARHGAP17 KO
CIP4-GFP
CIP4 KD
myc-ARHGAP17 + CIP4-GFP
ARHGAP17 KO + CIP4 KD
myc-ARHGAP17 + CIP4 KD
ARHGAP17 KO + CIP4-GFP
Cells with invadopodia (%)

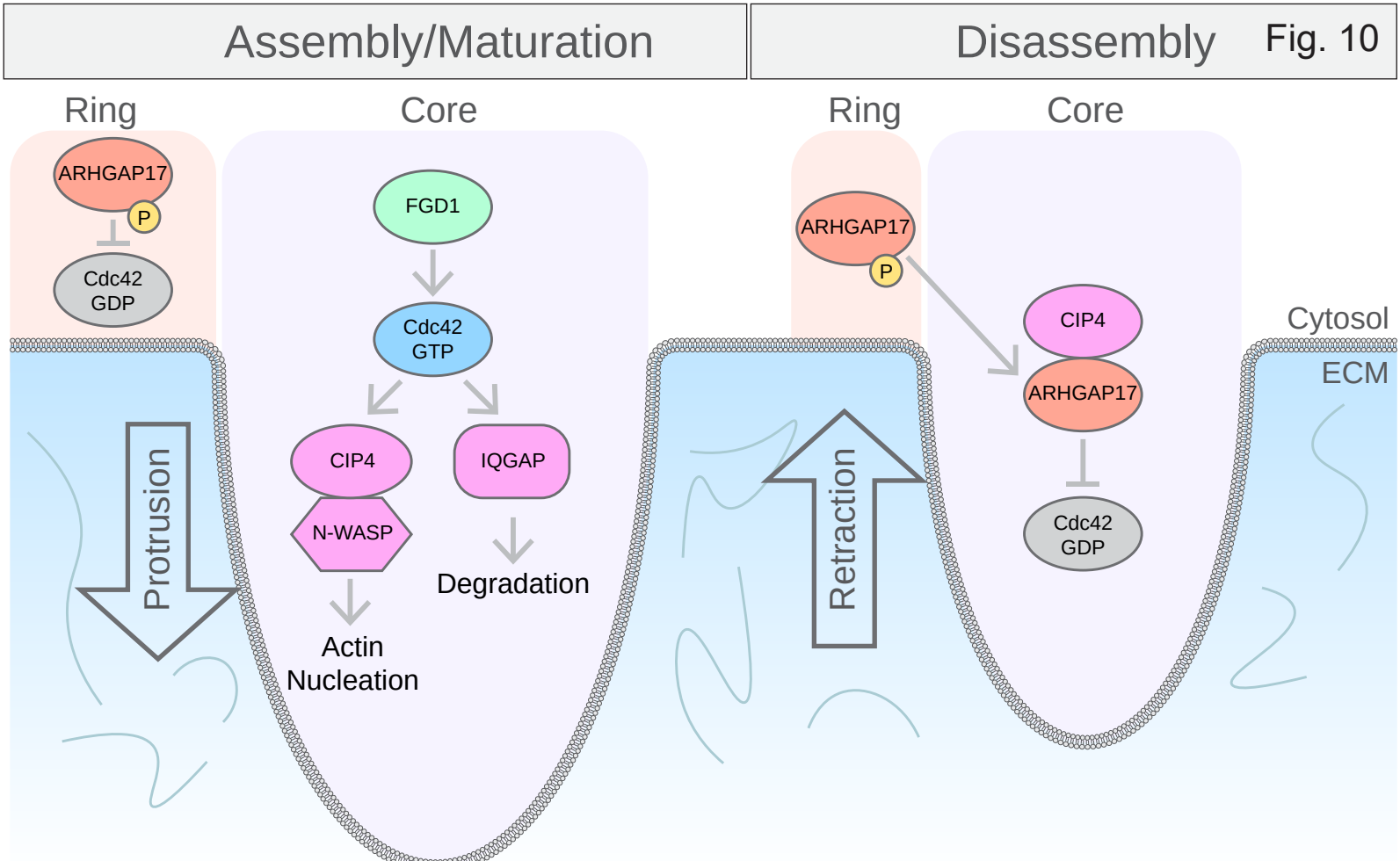
Assembly/Maturation
Disassembly
Fig. 10
Ring
Core
Ring
Core
ARHGAP17
P
Cdc42
GDP
FGD1
Cdc42
GTP
CIP4
N-WASP
IQGAP
Degradation
Actin
Nucleation
Protrusion
ARHGAP17
P
CIP4
ARHGAP17
Cdc42
GDP
Retraction
Cytosol
ECM

Fig. S1

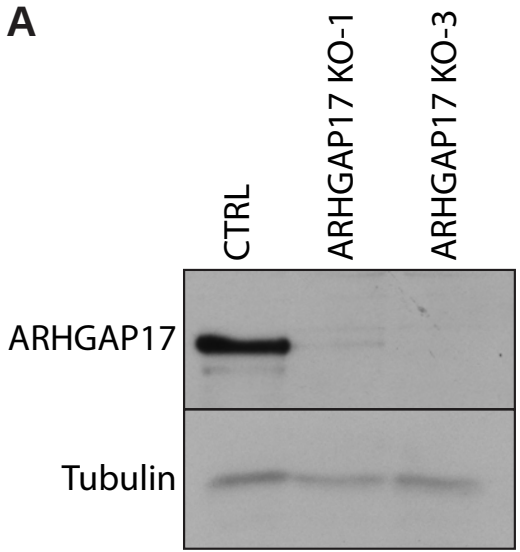
A
CTRL
ARHGAP17 KO-1
ARHGAP17 KO-3
ARHGAP17
Tubulin

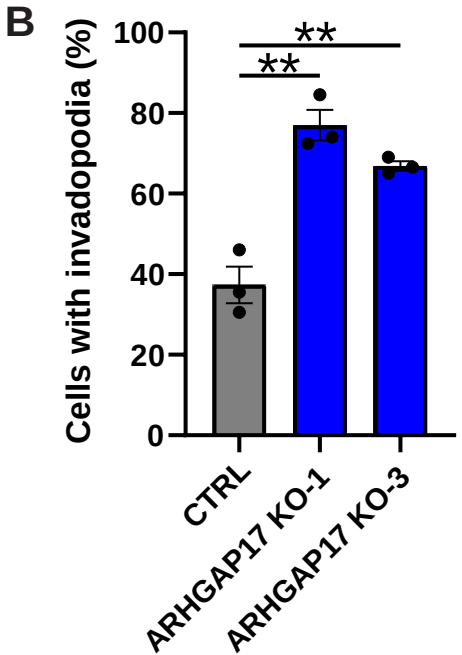
B
Cells with invadopodia (%)
100
80
60
40
20
0
**
**
CTRL
ARHGAP17 KO-1
ARHGAP17 KO-3

Fig. S2

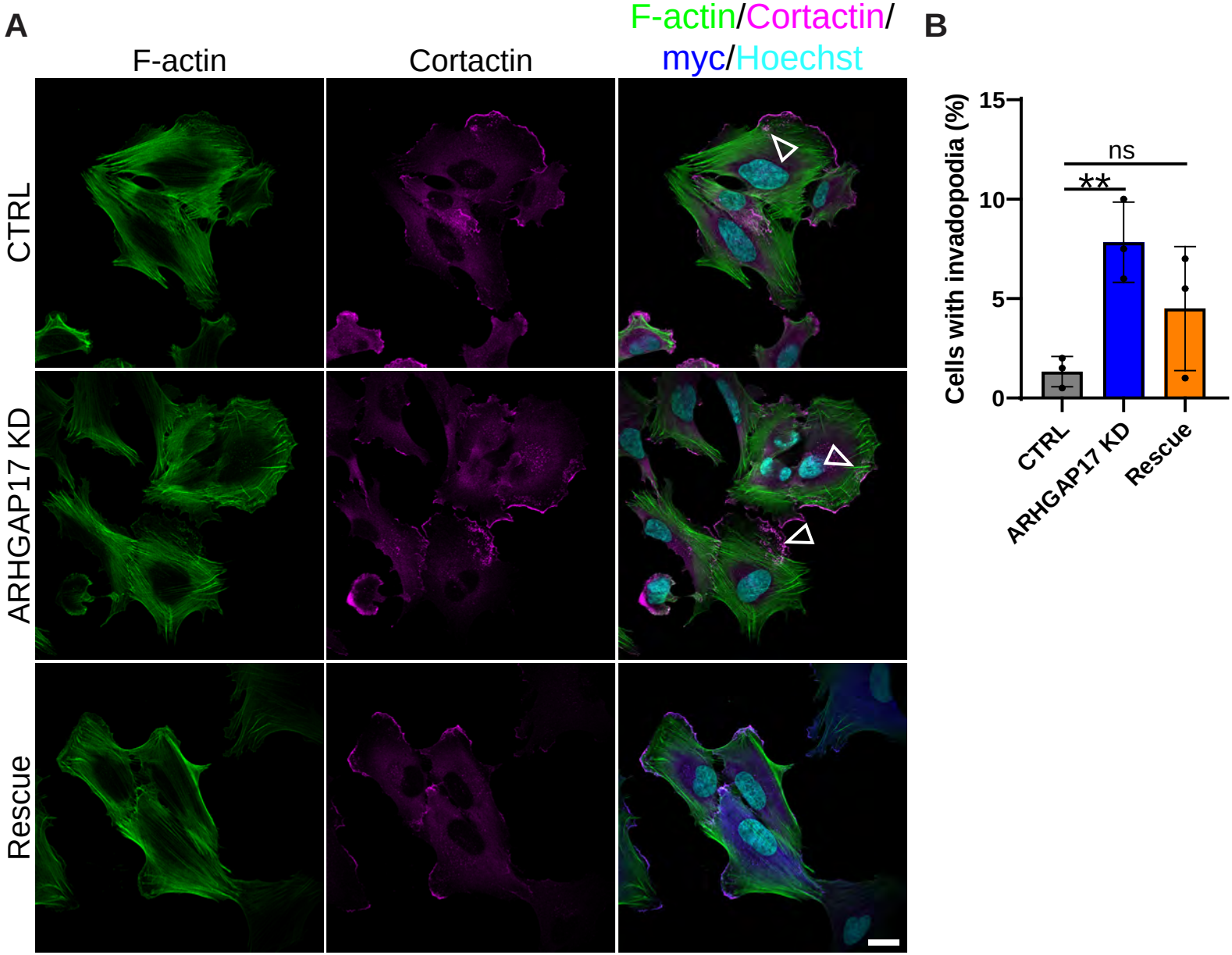
A
F-actin
Cortactin
F-actin/Cortactin/
myc/Hoechst
CTRL
ARHGAP17 KD
Rescue
B
Cells with invadopodia (%)
15
10
5
0
ns
**
CTRL
ARHGAP17 KD
Rescue

Fig. S3

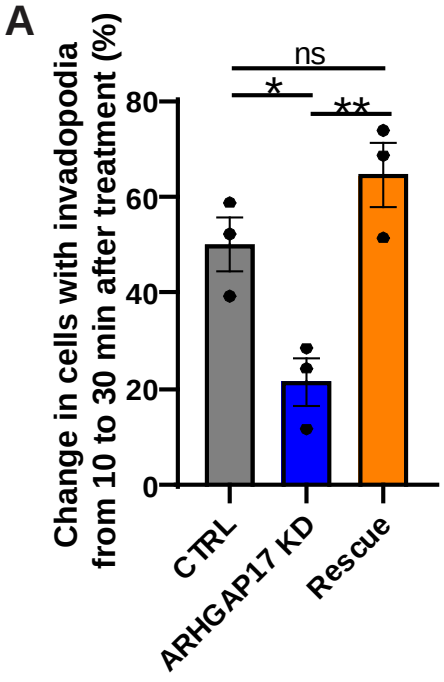
A
Change in cells with invadopodia from 10 to 30 min after treatment (%)
ns
*
**
80
60
40
20
0
CTRL
ARHGAP17 KD
Rescue

Fig. S4

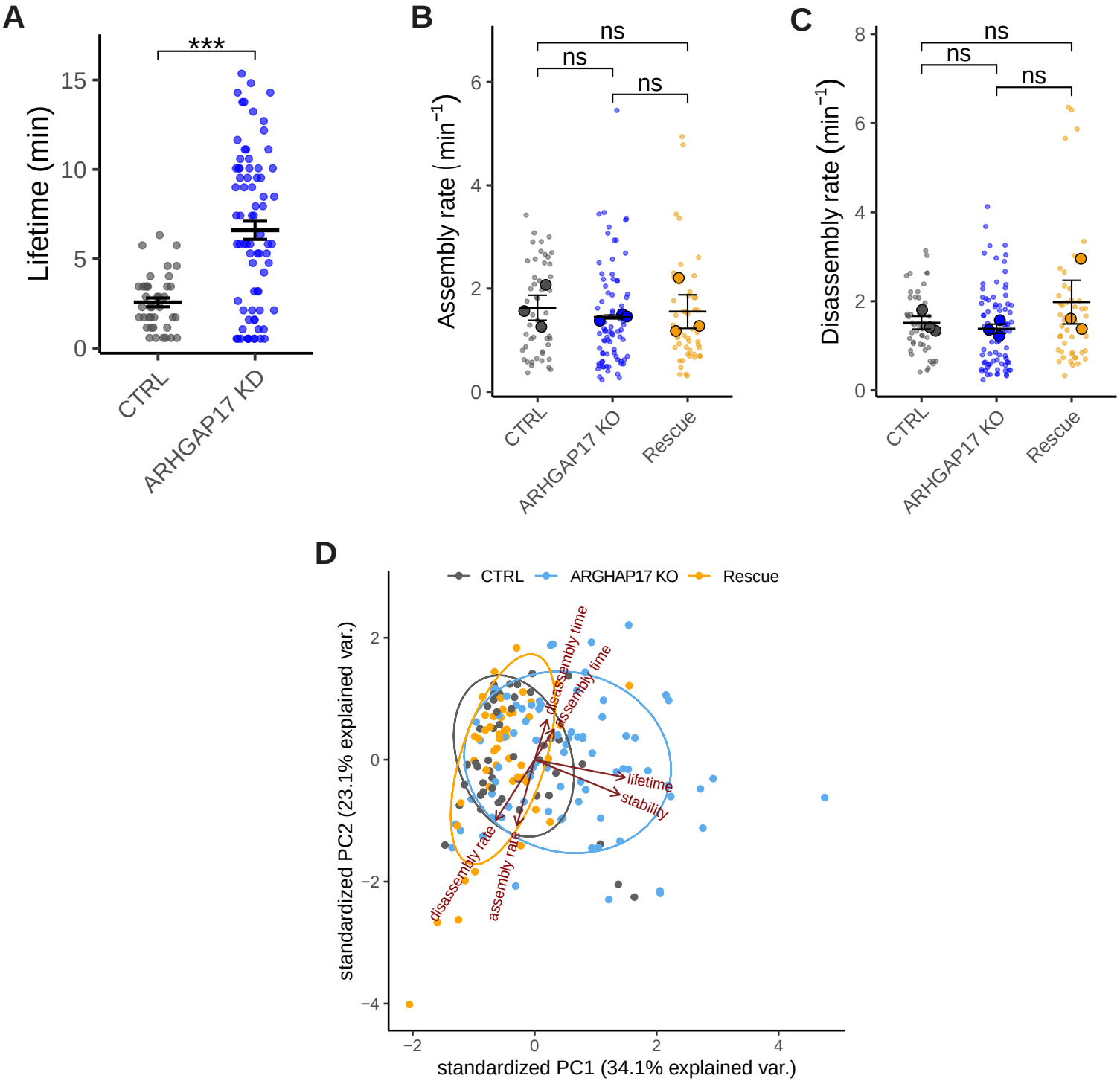
A
***
Lifetime (min)
15
10
5
0
CTRL
ARHGAP17 KD
B
ns
ns
ns
Assembly rate (min^{-1})
6
4
2
0
CTRL
ARHGAP17 KO
Rescue
C
ns
ns
ns
Disassembly rate (min^{-1})
8
6
4
2
0
CTRL
ARHGAP17 KO
Rescue
D
CTRL
ARGHAP17 KO
Rescue
disassembly time
assembly time
lifetime
stability
disassembly rate
assembly rate
standardized PC2 (23.1% explained var.)
2
0
−2
−4
−2
0
2
4
standardized PC1 (34.1% explained var.)

Fig. S5

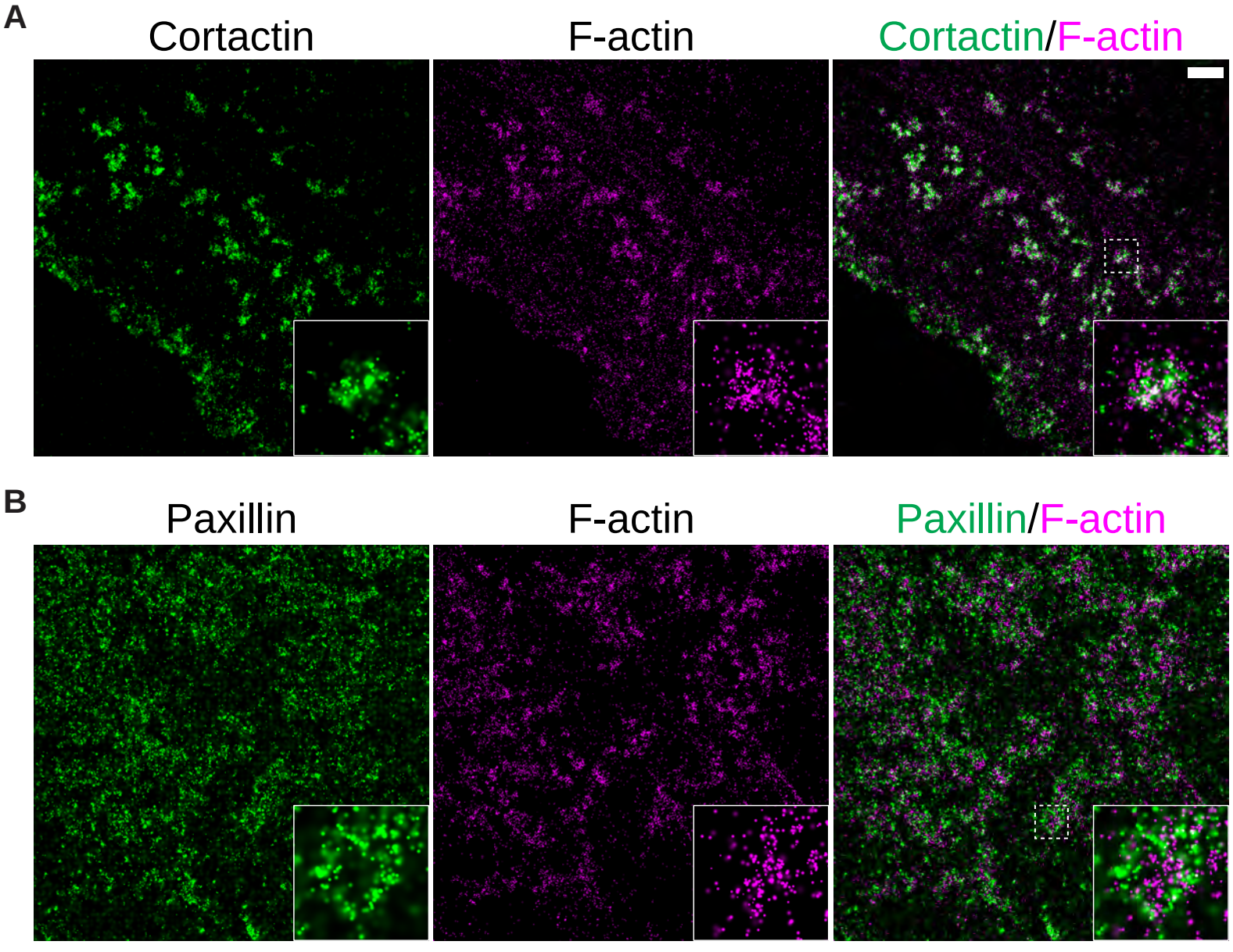
A
Cortactin
F-actin
Cortactin/F-actin
B
Paxillin
F-actin
Paxillin/F-actin

Fig. S6

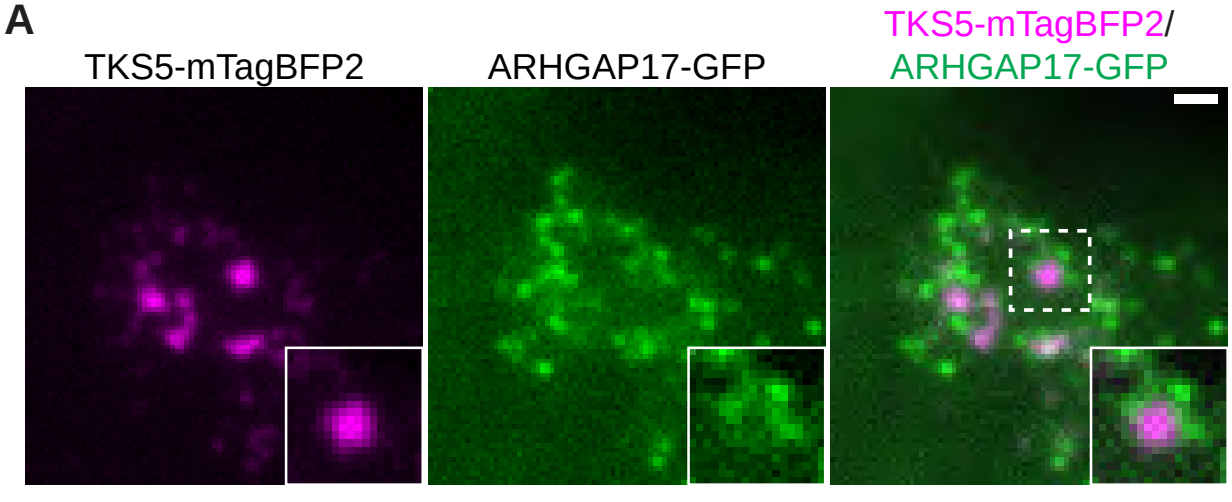
A
TKS5-mTagBFP2
ARHGAP17-GFP
TKS5-mTagBFP2/
ARHGAP17-GFP

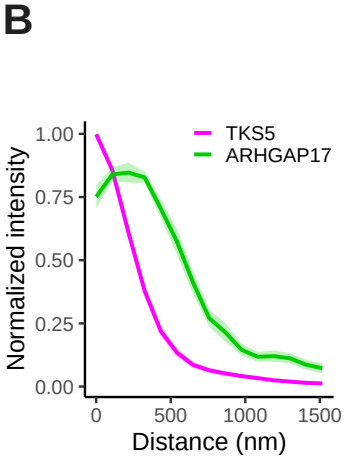
B
TKS5
ARHGAP17
Normalized intensity
1.00
0.75
0.50
0.25
0.00
0
500
1000
1500
Distance (nm)

Fig. S7

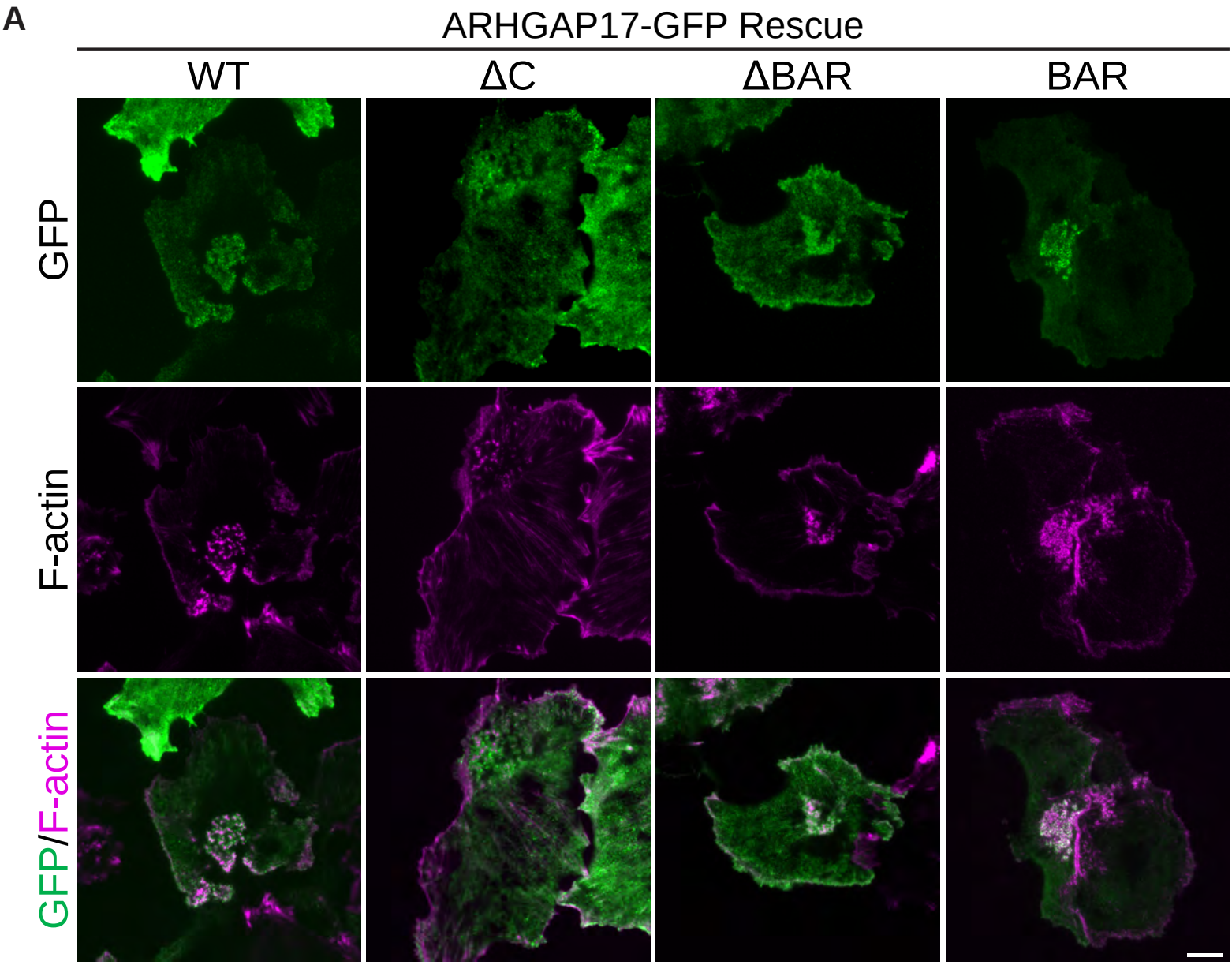

Fig. S8

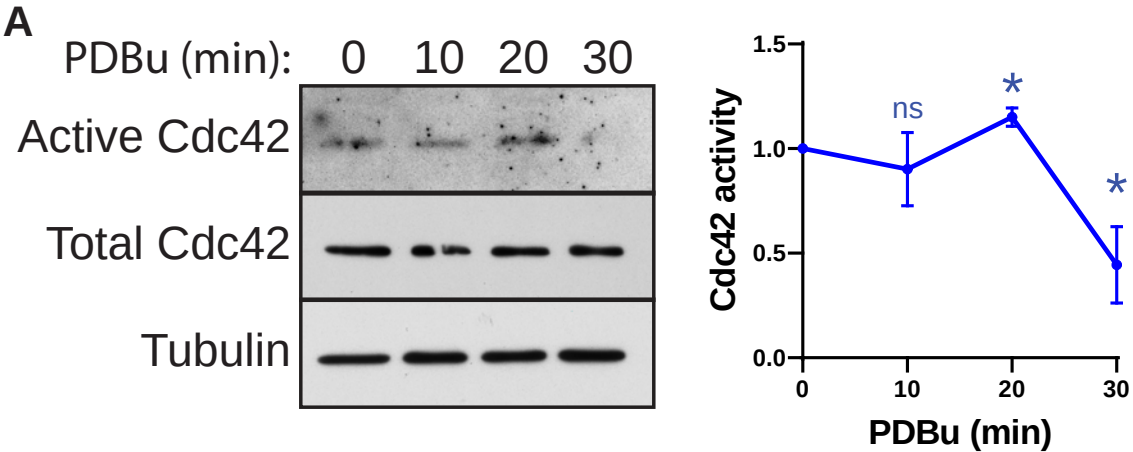
A
PDBu (min): 0 10 20 30
Active Cdc42
Total Cdc42
Tubulin
Cdc42 activity
1.5
1.0
0.5
0.0
ns
*
*
0
10
20
30
PDBu (min)

Fig. S9

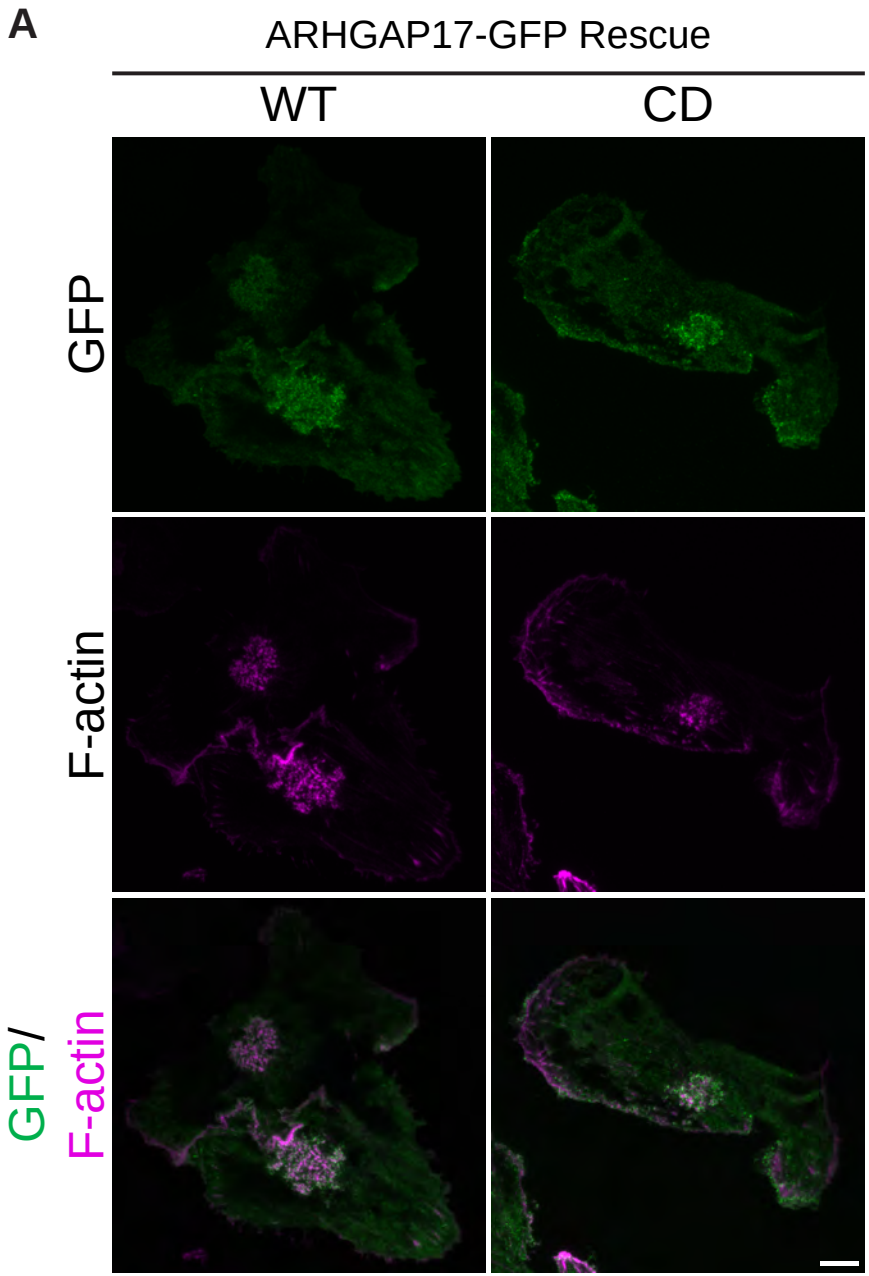

Fig. S10

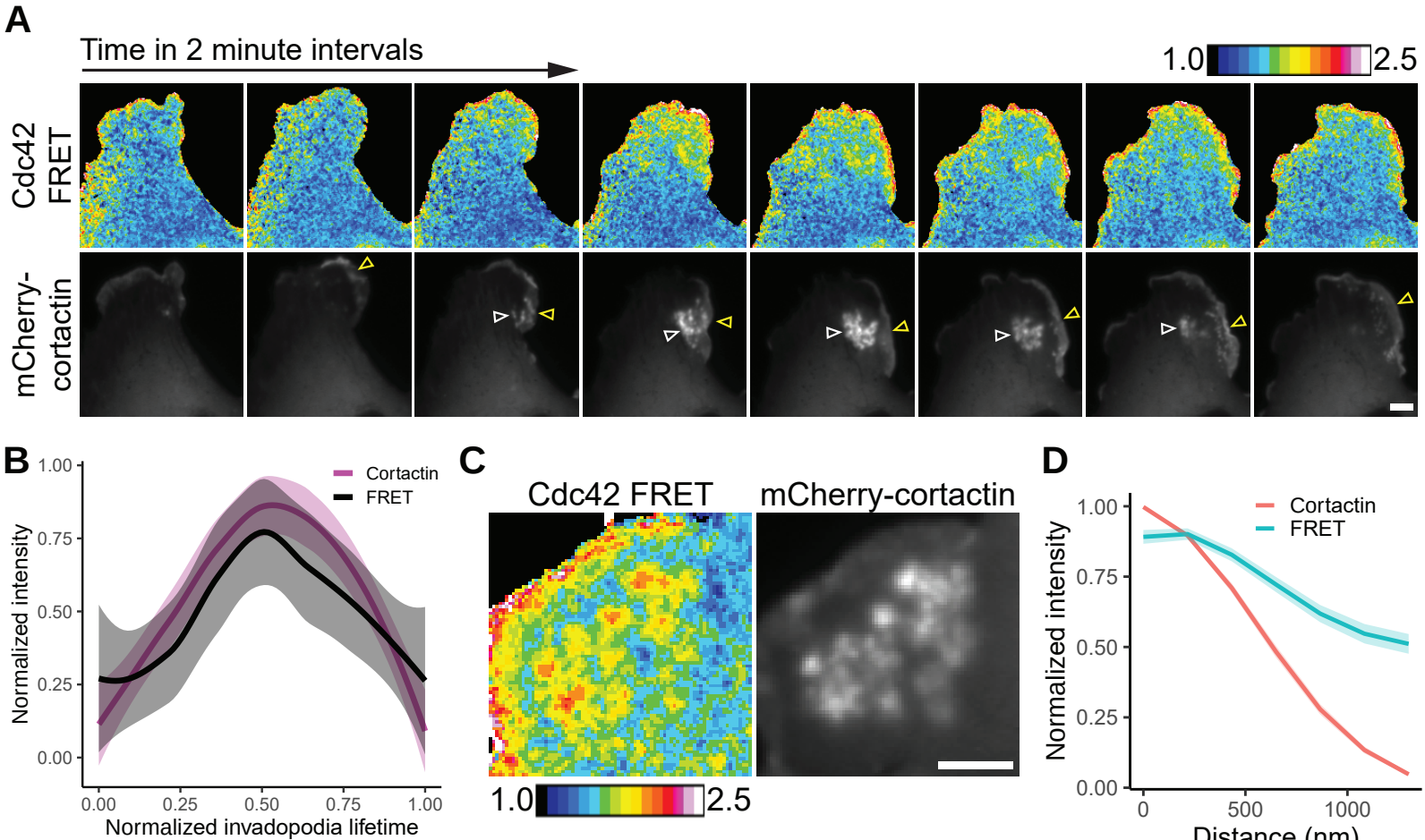
A
Time in 2 minute intervals
1.0
2.5
Cdc42 FRET
mCherry-cortactin
B
Cortactin
FRET
Normalized intensity
Normalized invadopodia lifetime
0.00
0.25
0.50
0.75
1.00
C
Cdc42 FRET
mCherry-cortactin
1.0
2.5
D
Cortactin
FRET
Normalized intensity
Distance (nm)
0
500
1000

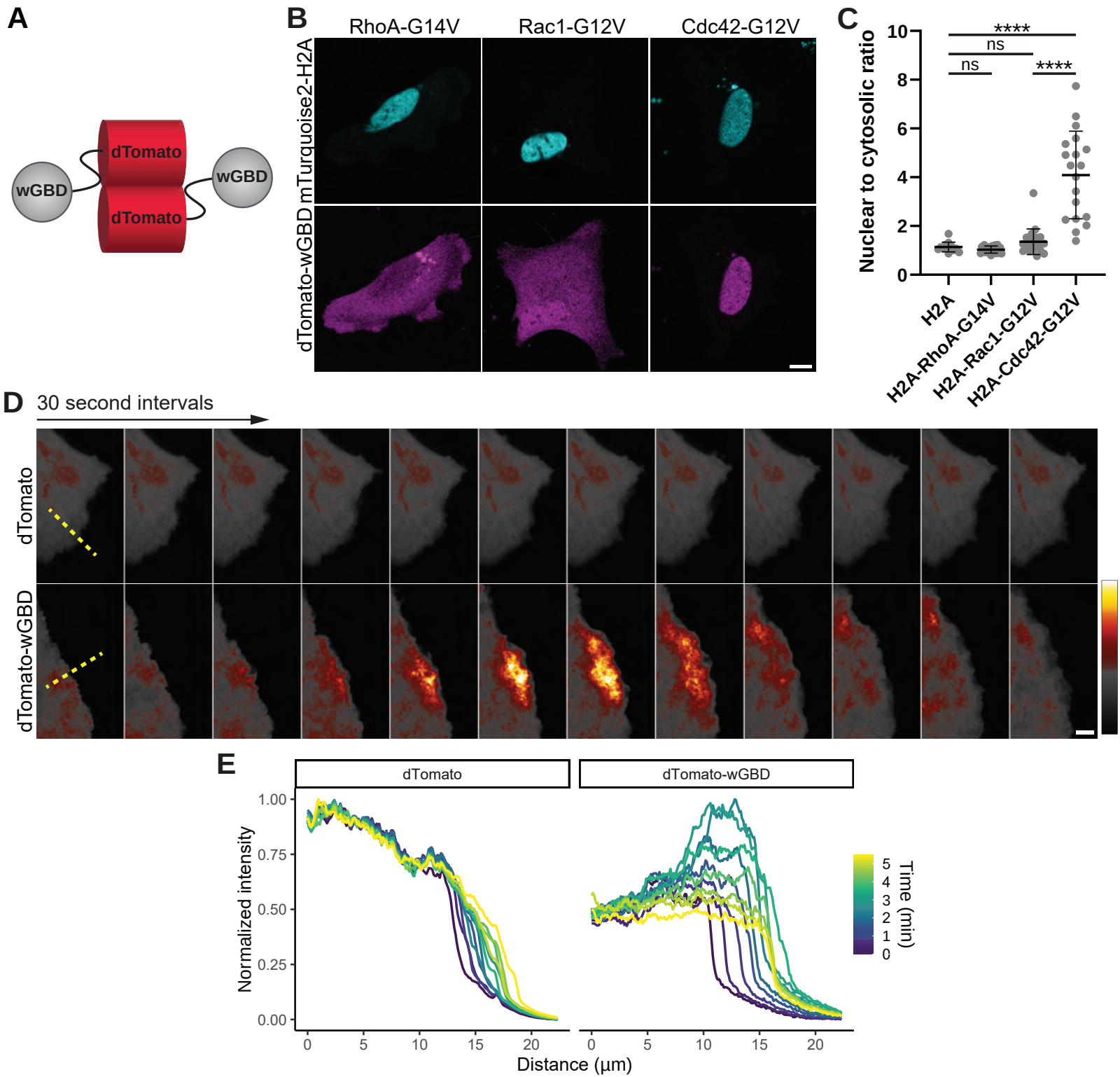
A
dTomato
wGBD
wGBD
dTomato
B
RhoA-G14V
Rac1-G12V
Cdc42-G12V
mTurquoise2-H2A
dTomato-wGBD
C
Nuclear to cytosolic ratio
****
ns
ns
****
H2A
H2A-RhoA-G14V
H2A-Rac1-G12V
H2A-Cdc42-G12V
D
30 second intervals
dTomato
dTomato-wGBD
E
dTomato
dTomato-wGBD
Normalized intensity
Distance (µm)
Time (min)
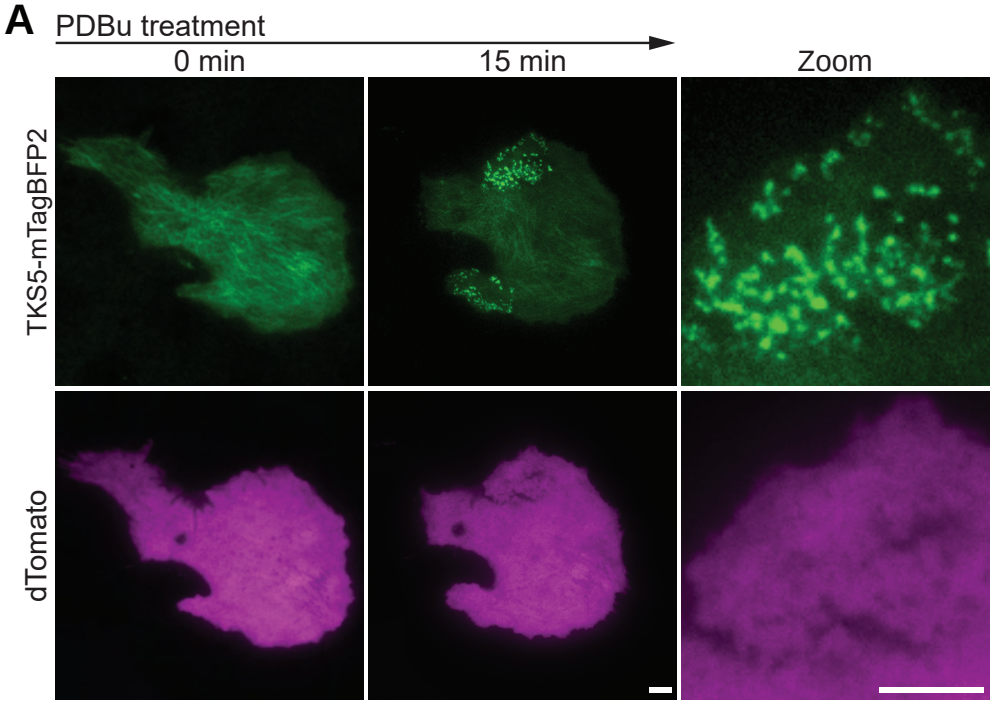
Fig. S12